

# Past and Future Climate Variability Uncertainties in the Global Carbon Budget using the MPI Grand Ensemble

Tammas Francis Loughran<sup>1,1</sup>, Lena R. Boysen<sup>2,2</sup>, Ana Bastos<sup>3,3</sup>, Kerstin Hartung<sup>4,4</sup>, Felix Havermann<sup>5,5</sup>, Hongmei Li<sup>2,2</sup>, Julia Esther Marlene Sophia Nabel<sup>2,2</sup>, Wolfgang A. Obermeier<sup>6,6</sup>, and Julia Pongratz<sup>3,3</sup>

<sup>1</sup>Ludwig Maximilian University

<sup>2</sup>Max Planck Institute for Meteorology

<sup>3</sup>Ludwig-Maximilians Universität

<sup>4</sup>Deutsches Zentrum für Luft- und Raumfahrt

<sup>5</sup>Dept. of Geography, Ludwig Maximilian University

<sup>6</sup>Faculty of Geosciences, Ludwig Maximilian University

November 30, 2022

## Abstract

Quantifying the anthropogenic fluxes of CO<sub>2</sub> is important to understand the evolution of carbon sink capacities, on which the required strength of our mitigation efforts directly depends. For the historical period, the global carbon budget (GCB) can be compiled from observations and model simulations as is done annually in the Global Carbon Project's (GCP) carbon budgets. However, the historical budget only considers a single realization of the Earth system and cannot account for internal climate variability. Understanding the distribution of internal climate variability is critical for predicting the future carbon budget terms and uncertainties. We present here a decomposition of the GCB for the historical period and the RCP4.5 scenario using single model large ensemble simulations from the Max Planck Institute Grand Ensemble (MPI-GE) to capture internal variability. We calculate uncertainty ranges for the natural sinks and anthropogenic emissions that arise from internal climate variability, and by using this distribution, we investigate the likelihood of historical fluxes with respect to plausible climate states. Our results show these likelihoods have substantial fluctuations due to internal variability, which are partially related to ENSO. We find that the largest internal variability in the MPI-GE stems from the natural land sink and its increasing carbon stocks over time. The allowable fossil fuel emissions consistent with 3°C warming may be between 9–18 PgCyr<sup>-1</sup>. The MPI-GE is generally consistent with GCP's global budgets with the notable exception of land-use change emissions in recent decades, highlighting that human action is inconsistent with climate mitigation goals.

**Past and Future Climate Variability Uncertainties in the Global Carbon Budget  
using the MPI Grand Ensemble**

**T. F. Loughran<sup>1</sup>, L. Boysen<sup>3</sup>, A. Bastos<sup>1,2</sup>, K. Hartung<sup>1,\*</sup>, F. Havermann<sup>1</sup>, H. Li<sup>3</sup>, J. E. M. S. Nabel<sup>3</sup>, W. A. Obermeier<sup>1</sup>, and J. Pongratz<sup>1,3</sup>**

<sup>1</sup>Dept. of Geography, Ludwig Maximilian University, Munich, Germany.

<sup>2</sup>Max Planck Institute for Biogeochemistry, Department of Biogeochemical Integration, Jena, Germany.

<sup>3</sup>Max Planck Institute for Meteorology, Hamburg, Germany.

\*Now at: Deutsches Zentrum für Luft- und Raumfahrt, Institut für Physik der Atmosphäre, Oberpfaffenhofen, Germany.

Corresponding author: Tamas Loughran (t.loughran@lmu.de)

**Key Points:**

- We use a single-model large ensemble to estimate uncertainties from internal climate variability in the global carbon budget.
- The land sink accounts for most internal climate uncertainty which may permit 9–18 PgCyr<sup>-1</sup> in allowable emissions by 2050 (for 3°C warming).

## 17 Abstract

18 Quantifying the anthropogenic fluxes of CO<sub>2</sub> is important to understand the evolution of carbon  
 19 sink capacities, on which the required strength of our mitigation efforts directly depends. For the  
 20 historical period, the global carbon budget (GCB) can be compiled from observations and model  
 21 simulations as is done annually in the Global Carbon Project's (GCP) carbon budgets. However,  
 22 the historical budget only considers a single realization of the Earth system and cannot account  
 23 for internal climate variability. Understanding the distribution of internal climate variability is  
 24 critical for predicting the future carbon budget terms and uncertainties. We present here a  
 25 decomposition of the GCB for the historical period and the RCP4.5 scenario using single model  
 26 large ensemble simulations from the Max Planck Institute Grand Ensemble (MPI-GE) to capture  
 27 internal variability. We calculate uncertainty ranges for the natural sinks and anthropogenic  
 28 emissions that arise from internal climate variability, and by using this distribution, we  
 29 investigate the likelihood of historical fluxes with respect to plausible climate states. Our results  
 30 show these likelihoods have substantial fluctuations due to internal variability, which are  
 31 partially related to ENSO. We find that the largest internal variability in the MPI-GE stems from  
 32 the natural land sink and its increasing carbon stocks over time. The allowable fossil fuel  
 33 emissions consistent with 3°C warming may be between 9–18 PgCyr<sup>-1</sup>. The MPI-GE is generally  
 34 consistent with GCP's global budgets with the notable exception of land-use change emissions in  
 35 recent decades, highlighting that human action is inconsistent with climate mitigation goals.

## 36 1 Introduction

37 The global carbon budget of CO<sub>2</sub> can be decomposed into anthropogenic emissions and natural  
 38 sinks. Anthropogenic emissions are mostly due to fossil fuel burning and fossil carbonates ( $E_{FF}$ ),  
 39 but also from land-use induced land cover change and land management (“land-use change  
 40 emissions” in the following,  $E_{LUC}$ ). The emitted CO<sub>2</sub> is then distributed into three natural sinks: it  
 41 is either assimilated by the land surface via ecosystem productivity ( $S_{LAND}$ ), absorbed by the  
 42 ocean via diffusion and photosynthesis of marine organisms ( $S_{OCEAN}$ ), or accumulated in the  
 43 atmosphere (atmospheric growth:  $G_{ATM}$ ) leading to increased atmospheric CO<sub>2</sub> concentrations  
 44 (Le Quéré et al. 2013; Friedlingstein et al. 2020).

45 One of the key goals of the Global Carbon Project (GCP) is to evaluate anthropogenic  
 46 perturbations on the global carbon cycle and to understand the response of the natural carbon  
 47 sinks to increasing fossil emissions and land-use changes (e.g. Friedlingstein et al. 2020; Le  
 48 Quéré et al. 2018a,b). These global carbon budgets, conducted almost every year since 2007  
 49 (Canadell et al. 2008), provide an important understanding of the efficiency and potential  
 50 saturation of the natural sinks. This in turn is essential knowledge for predicting the future sink  
 51 capacities and, therefore, the required strength for future climate mitigation targets and of  
 52 “allowable” emissions under given climate targets. A comprehensive understanding of  
 53 uncertainties in these budgets is essential for guiding policy and decision-making.

54 The components of the GCP carbon budgets are associated with large uncertainties,  
 55 which are based on a combination of observation and model uncertainties. Fossil emissions are  
 56 based on energy and fuel consumption data whereby the uncertainties lie in the fuel  
 57 consumption, fuel carbon content, and combustion efficiency (Andres et al. 2012). The  $E_{LUC}$   
 58 estimate is based on three bookkeeping models, in which estimates of land-use transitions are  
 59 combined with observation-based carbon densities to track terrestrial emissions and removals

according to empirical temporal response curves for each ecosystem (Hansis et al. 2015; Houghton and Nassikas 2017). The corresponding estimates for  $E_{LUC}$  uncertainty have low confidence and are based on expert knowledge, which considers the bookkeeping models and the range of the 17 global dynamical vegetation models (DGVMs) (Friedlingstein et al. 2020). The ocean sink estimate is based on the standard deviation of nine global ocean biogeochemical models and their consistency with observed  $CO_2$  partial pressure-based flux estimates. The terrestrial sink in earlier budgets was estimated as a residual from all other terms or based on DGVMs from the 2019 budget onwards. The estimates of both  $S_{LAND}$  and  $S_{OCEAN}$  are evaluated to have medium confidence (Friedlingstein et al. 2020). When estimating the land sink with DGVMs, the  $G_{ATM}$  cannot be matched, leading to a “budget imbalance” term of  $\sim 0.4 \text{ Pg C yr}^{-1}$ . While atmospheric measurements of  $CO_2$  concentration are relatively more accurate, there are substantial interannual variations (IAV) driven by natural climate variability (Dlugokencky and Tans 2018; Conway et al. 1994).

From such global carbon budgets, it is possible to quantify the future emissions to stay within a given trajectory of climate change (Rogelj et al. 2016, Millar et al. 2016). However, estimating these “allowable emissions” from historical budgets actually requires considering an additional source of uncertainty: the internal variability of the climate system. The uncertainties in the GCP budgets are related to observational and model uncertainties while uncertainties associated with internal climate variability are not directly addressed.

Much of the IAV in  $CO_2$  concentration and its impacts on the regional (Zhu et al. 2018) and global carbon sinks (Bastos et al. 2013, Ballantyne et al. 2012) is driven by internal variability in the climate system. Internal variability arises from stochastic processes and feedbacks in the coupled ocean-atmosphere system (e.g. El Niño–Southern Oscillation; ENSO) and is difficult to predict due to high sensitivity to initial conditions and the chaotic evolution of the Earth system (Deser et al. 2012). Traditionally, internal variability in weather and climate forecasts is accounted for by performing ensemble forecasting, i.e. running multiple simulations of the same (or several) models started from perturbed initial conditions, in order to estimate the distribution of future climate states (Deser et al. 2012).

The importance of considering the full range of potential climate states due to internal climate variability is particularly pertinent to future estimates of the carbon budget, where the exact climate state (and consequently the strength of the natural sinks) in a given year is unknown. Using only one realization may not robustly capture these future states. Furthermore, we cannot assume that the variance of the natural  $CO_2$  fluxes is stationary under increasing atmospheric  $CO_2$ . It is not possible to estimate the range of plausible carbon budget fluxes due to internal climate variability using only one instance of historical observations or observationally forced model simulations. Using ensemble simulations will allow for a more robust calculation of future trends in the mean and variability of the carbon budget terms (e.g. Kay et al. 2015).

Since the historical observation-based carbon budget uncertainty only considers one realization of internal climate variability, the influence of internal climate variability on each budget term is unknown. Therefore, we ask the following research questions:

- How large is the uncertainty from internal climate variability in the global carbon budget terms and how does it compare to the variability of the latest global carbon budget (GCB2020) values?

- How likely were the historical carbon fluxes with respect to the distribution of possible fluxes from internal climate variability and what drove those anomalies?
- How will the carbon budget components and their internal variability change in the future (e.g. under RCP4.5)?

In this study, we estimate uncertainties associated with internal climate variability for each component of the carbon budget using a large ensemble of single-model simulations from the Max Planck Institute Grand Ensemble project (MPI-GE; Maher et al. 2019). We compare the results of the estimates for internal climate variability uncertainties to the uncertainties of the recent GCB2020 (Friedlingstein et al. 2020). Furthermore, we discuss the suitability and possible limitations of using a large ensemble of simulations for better understanding variability and uncertainties associated with  $E_{LUC}$  and  $S_{LAND}$  and how many ensemble members are required to answer these questions.

## 2 Methods

### 2.1 Overview of models and simulations

The methods used to generate the ensemble of climate realizations as part of the MPI-GE project are fully described in Maher et al. (2019). Therefore, we only give a summary here. The MPI-GE is a single model large ensemble project that uses the Max Planck Institute Earth System Model (MPI-ESM; for a full description see Giorgetta et al. 2013) version 1.1. The MPI-ESM is composed of an atmospheric component provided by ECHAM 6.3.01p3 (Stevens et al. 2013) run at T63L47 resolution ( $\sim 1.8^\circ$  and 47 vertical layers), an ocean component provided by MPIOM 1.6.1p1 (Marsland et al. 2003) run at GR15L40 resolution ( $\sim 1.5^\circ$ ), the ocean biogeochemistry model HAMOCC5.2 (Ilyina et al. 2013), and the land component JSBACH3 (Reick et al. 2013, Goll et al. 2015). 100 ensemble members are generated by branched initialization (every  $\sim 6$ –24 years) from a sub-sample of years from a pre-industrial control (piControl) simulation. The piControl as well as the subsequent historical and future simulations follow the protocol of concentration-driven Earth system model runs of the Coupled Model Intercomparison projects (CMIP), in this case specifically CMIP5 (Taylor et al. 2012).

The JSBACH3 component simulates transitions in land cover types with respect to both natural vegetation dynamics and land-use changes. However, we utilize a smaller standalone sub-component of JSBACH3 called Carbon Balance ALONE (CBALONE) to differentiate the emissions due to land-use change from the remaining net land sink (as is done in e.g. Roeckner et al. 2010). As in all Earth system model simulations that perform historical or scenario simulations, anthropogenic and natural effects occur concurrently, i.e. the simulations only provide the net land-atmosphere exchange (i.e.  $S_{LAND} + E_{LUC}$ ). Only instantaneous emissions to the atmosphere can be derived directly from the historical or scenario simulations (as, e.g., in Lawrence et al. 2012). These, however, neglect legacy emissions that result in particular from the slow decay of wood products, harvested material left on site, and the adjustment of soil carbon stocks to the altered land-use over decades to centuries, but also comprise slow carbon uptake in processes like forest regrowth. In order to capture all fluxes from land-use change (instantaneous and legacy), additional simulations are essential that exclude the land-use change forcing, such that by difference to the historical or scenario simulation  $E_{LUC}$  can be isolated (Pongratz et al., 2014). Note that effects of altered atmospheric  $CO_2$  concentrations by  $E_{LUC}$ , with emissions creating a compensating carbon sink in land and ocean (the “land-use feedback”), are excluded

in our concentration-driven feedback (Pongratz et al. 2014). Similarly, since CBALONE is driven with the climate from the coupled simulation, changes in surface climate due to land-use change also act the same way in both simulations. Thus, the difference between the simulations with (MPI-GE) and without land-use change (CBALONE) cancels these effects (apart from secondary-order terms) and excludes resulting feedbacks. This is essential to make our estimates consistent with the methodology used in the GCB2020 for the terrestrial budget terms.

CBALONE includes only the long-term dynamics associated with carbon turnover rates and vegetation biogeography. We force CBALONE with daily data from 100 climate realizations taken from the MPI-GE, both with and without anthropogenic land-use change (LUC and noLUC simulations respectively) comparable to the approach taken by the GCP (Friedlingstein et al. 2020). The land-use change transition data utilized by MPI-GE and CBALONE are taken from the Land Use Harmonization 2 project (LUH2; Hurtt et al. 2011). While the carbon fluxes from CBALONE did not exactly match JSBACH3 estimates, they consistently simulate JSBACH3 fluxes to within 5% accuracy (Figure S6). Therefore, the CBALONE simulations with land-use change are required so that  $E_{LUC}$  could be calculated independent of the small CBALONE error (in absence of the error, the net land-atmosphere exchange could have been directly provided by the MPI-GE simulations).

The climate realizations used to force CBALONE were taken from existing daily output from the MIP-GE historical and RCP4.5 scenarios (1850–2099; Table 1). We chose the RCP4.5 scenario as a scenario of medium climate change that estimates the CO<sub>2</sub> emissions under climate policies designed to limit global warming to no more than 3°C over present-day temperatures, allowing us to create uncertainty estimates of fossil emissions that are consistent with this goal. The daily model output variables that are used to force CBALONE include 2m air temperature, soil temperature, precipitation, net primary productivity (NPP) per plant functional type (PFT), leaf area index (also per PFT), and maximum wind. These variables are marked as “environmental” in Figure 1.

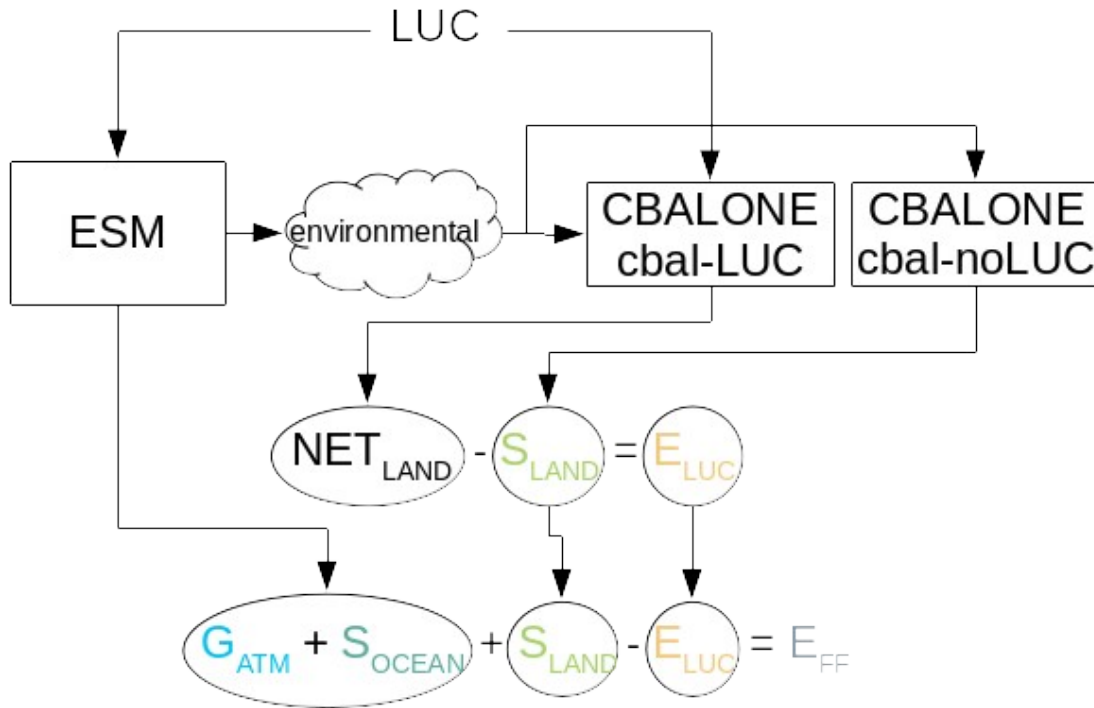


**Figure 1.** Workflow schematic for simulations and carbon budget decomposition for each ensemble member. Variables from MPI-GE labeled “*environmental*” include leaf area index, net primary productivity, topsoil temperature, maximum 10m wind speed, air temperature and precipitation (see section 2.2).

**Table 1.** Experiment simulations. Each experiment has 100 ensemble members. The MPI-GE simulations have been labeled with the prefix “mpige”, while the CBALONE simulations are labeled as “cbal”. The scenarios are labeled with the suffix “hist” for the historical scenario and “rcp4.5” for the future scenario. Both scenarios for CBALONE are simulated with land-use change (labeled with LUC) and without land-use change using 1850 land-use throughout the simulation (labeled with noLUC). There are only 97 ensemble members for the CBALONE RCP4.5 scenario because a few MPI-GE output files required by CBALONE contained erroneous data.

	LUC	No LUC
<b>Historical (1850–2005)</b>	mpige-LUC-hist cbal-LUC-hist	cbal-noLUC-hist
<b>RCP 4.5 (2006–2099)</b>	mpige-LUC-rcp4.5 cbal-LUC-rcp4.5	cbal-noLUC-rcp4.5

## 2.2 Carbon budget decomposition

The carbon budget is decomposed here into various source and sink terms as in Friedlingstein et al. (2019), utilizing output from the MPI-GE and the CBALONE simulations. The monthly CBALONE output is aggregated to annual values for comparison to the GCB2020. The cbal-noLUC simulation provides land-atmosphere exchange that would occur without land-use changes, and thus  $S_{LAND}$  is calculated as the net biome productivity (NBP) from this simulation. Equation 1 clarifies components of NBP taken from the model, where NPP is net primary productivity, RH is heterotrophic respiration, fFire is carbon flux due to wildfires, fHarvest is carbon flux due to crop and wood harvest, fGrazing is carbon flux due to herbivorous grazing, and fLCC is the instantaneous emissions from land-use induced land cover changes. The fLCC term is zero in the cbal-noLUC simulations.

$$NBP = S_{LAND} = NPP + RH + fFire + fHarvest + fGrazing + fLCC \quad (1)$$

$E_{LUC}$  is calculated as the difference in NBP between the cbal-LUC and cbal-noLUC simulations (Equation 2; note that fluxes to the natural sinks are negative values and fluxes to the atmosphere are positive consistent with Friedlingstein et al. 2020). Correspondingly, the NBP from the cbal-LUC simulation is equivalent to the net land-atmosphere exchange ( $NET_{LAND}$ ).

$$E_{LUC} = NBP|_{cbal-LUC} - NBP|_{cbal-noLUC} = NET_{LAND} - S_{LAND} \quad (2)$$

$G_{ATM}$  and  $S_{OCEAN}$  are taken directly from the MPI-GE output. The implied “compatible” emissions (also  $E_{FF}$ ) are calculated as the residual of all other terms in the budget (Equation 3 & Figure 1), as described in Roeckner et al. (2010) and Jones et al. (2013). These are the emissions that would need to occur for  $CO_2$  to be conserved given particular atmospheric concentration, land-use emissions, and natural sink fluxes. This is different from the GCB2020 approach, where all terms were determined independently based on model or observational estimates, which requires a budget imbalance term to be added.

$$E_{FF} + E_{LUC} = G_{ATM} + S_{OCEAN} + S_{LAND} \quad (3)$$

We calculated the full decomposition of the carbon budget for each ensemble member of the historical and RCP4.5 scenarios and compare it to the GCB2020 (Friedlingstein et al. 2020) as the best estimate of the real global carbon cycle. Decadal averages of the MPI-GE ensemble mean and standard deviation are calculated for a direct comparison with the decadal mean and uncertainties presented in the GCB2020. To assess the magnitude of the uncertainties due to internal climate variability compared to the magnitude of the budget terms, we further calculate the signal-to-noise ratio (SNR) of each term as the ensemble mean divided by the ensemble standard deviation.

## 2.3 Interannual variability

While internal climate variability may contribute to interannual variations in carbon fluxes to the natural sinks, there are also variations driven by non-internal climate related factors, for example changes in anthropogenic activity ( $E_{FF} + E_{LUC}$ ) and volcanism. An assessment of uncertainties based on temporal standard deviations would be a mixture of internal and non-internal



variability, while an ensemble standard deviation at a given time step would reflect variations only due to internal climate variability. In order to assess future uncertainties, it is important that the model can simulate historical IAV appropriately. Here we assess the ability of individual MPI-GE and CBALONE ensemble members to adequately represent the temporal standard deviation of the historical year-to-year climate variations in each GCB2020 budget term. Therefore, we define a reference IAV as the temporal standard deviation of annual fluxes over the base period 1961–1990 (World Meteorological Organization standard reference period). All models have unique imperfections in their ability to simulate the statistical properties of the carbon fluxes such as mean and standard deviation, which we refer to as model bias. Furthermore, each may have a different trend over the base period which would artificially alter the IAV. To remove the model biases in the ensemble mean of the MPI-GE, we detrend the budget terms of each ensemble member before calculating IAV using an ordinary least-squares regression (OLR) of the ensemble mean over the historical period 1959–2005. We also detrended each model used in the GCB2020 and calculate the IAV over the same period.

#### 2.4 Probability of exceedance of past budget terms

To evaluate how likely past carbon fluxes were compared to the range of possible climate states due to internal variability, we describe here a measure of the probability of exceedance. Supposing a relatively small amount of CO<sub>2</sub> uptake by the land surface in a particular year, it is quite likely that under more favorable climate conditions for carbon storage this land CO<sub>2</sub> uptake would be exceeded. Therefore, we aim to calculate the probability that the MPI-GE members are greater than the GCB2020 multi-model mean (which we assume to be the closest estimate to historical CO<sub>2</sub> fluxes). Each budget term for the MPI-GE and GCB2020 is OLR detrended in the same way as described above (Section 2.3) except that we use the 1959–2018 period (i.e. the longest available common period for GCB2020 and the MPI-GE simulations). For each year and budget term, we calculate the corresponding cumulative distribution functions (“exceedance”) of the MPI-GE ensemble members using a kernel density estimator (Scott 2015). We then evaluate the GCB2020 terms on the complement of the cumulative distribution functions ( $1 - \text{Pr.}$ ) to find their occurrence probability (e.g. see Figure S3). Since we use a cumulative distribution, the complement probability is the “exceedance probability” of the ensemble spread being larger than the historical value. Unusually large historical fluxes will therefore have low probability of exceedance. This is similar to the probability of exceedance calculations from studies on climate extremes (e.g. Suarez-Gutierrez et al. 2020).

Finally, we assess the relationship of the GCB2020 exceedance probabilities for  $S_{\text{LAND}}$  and  $S_{\text{OCEAN}}$  fluxes to ENSO, since this is the most prominent mode that drives internal climate variability (Dannenbergh et al. 2015; Zhang et al. 2019). We use the annual mean Niño 3.4 index from the NOAA Climate Prediction Center (Climate Prediction Center 2017) which uses ERSST V5 (Huang et al. 2017) sea surface temperatures averaged over the region 5°N–5°S, 170–120°W. We then calculate the Pearson’s correlation coefficient and the OLR between the exceedance probabilities of the natural sinks and the Niño 3.4 index. We test the significance of this correlation using a two-sided t-test under the null hypothesis that a relationship between the exceedance probabilities of the GCB2020 fluxes and ENSO state can be rejected at the 95% confidence level. Since these methods assume normally distributed data, we beforehand tested the normality of the budget terms and their probabilities using the Shapiro-Wilk test for normality (Shapiro and Wilk, 1965). We found that all budget terms (except for  $G_{\text{ATM}}$ ) are normally distributed in the 1850–2018 period.

## 3 Results

### 3.1 Temporal evolution of budget components and internal climate variability uncertainties

The historical period and RCP4.5 scenario have globally increasing CO<sub>2</sub> fluxes from the atmosphere to the land and ocean sinks until about 2040 before decreasing thereafter (see Figure 2) due to assumed RCP4.5 mitigation measures. The decrease in land and ocean sink is because  $G_{\text{ATM}}$  in RCP4.5 decelerates after 2040 resulting in an atmospheric concentration of ~525 ppm CO<sub>2</sub> by 2100 (Thomson et al. 2011). The compatible fossil emissions in the MPI-GE ( $E_{\text{FF}}$  in Figure 2) share similar temporal evolution of the natural sinks. On the other hand,  $E_{\text{LUC}}$  is driven by the LUH2 land-use data set and is independent of fossil emissions, which increases until about 1990 before becoming a weak net sink from around 2020 onward under the RCP4.5 scenario (Figure 2 and S1 b). Within the period 1970–2010, the ensemble means of the  $G_{\text{ATM}}$  and  $E_{\text{FF}}$  terms show annual to decadal-scale variations, which are a known feature of the CO<sub>2</sub> concentration forcing used in the historical period (caused by the introduction of additional CO<sub>2</sub> observation stations in the 1960s, see Figure 10 of Meinshausen et al. 2017) and are not internally driven variations in the MPI-ESM. The  $S_{\text{LAND}}$  and  $S_{\text{OCEAN}}$  do not immediately respond to such rapid changes in  $G_{\text{ATM}}$  since they are dominated by the climate state and its variability. It then follows that these variations are evident in the residual  $E_{\text{FF}}$  term.

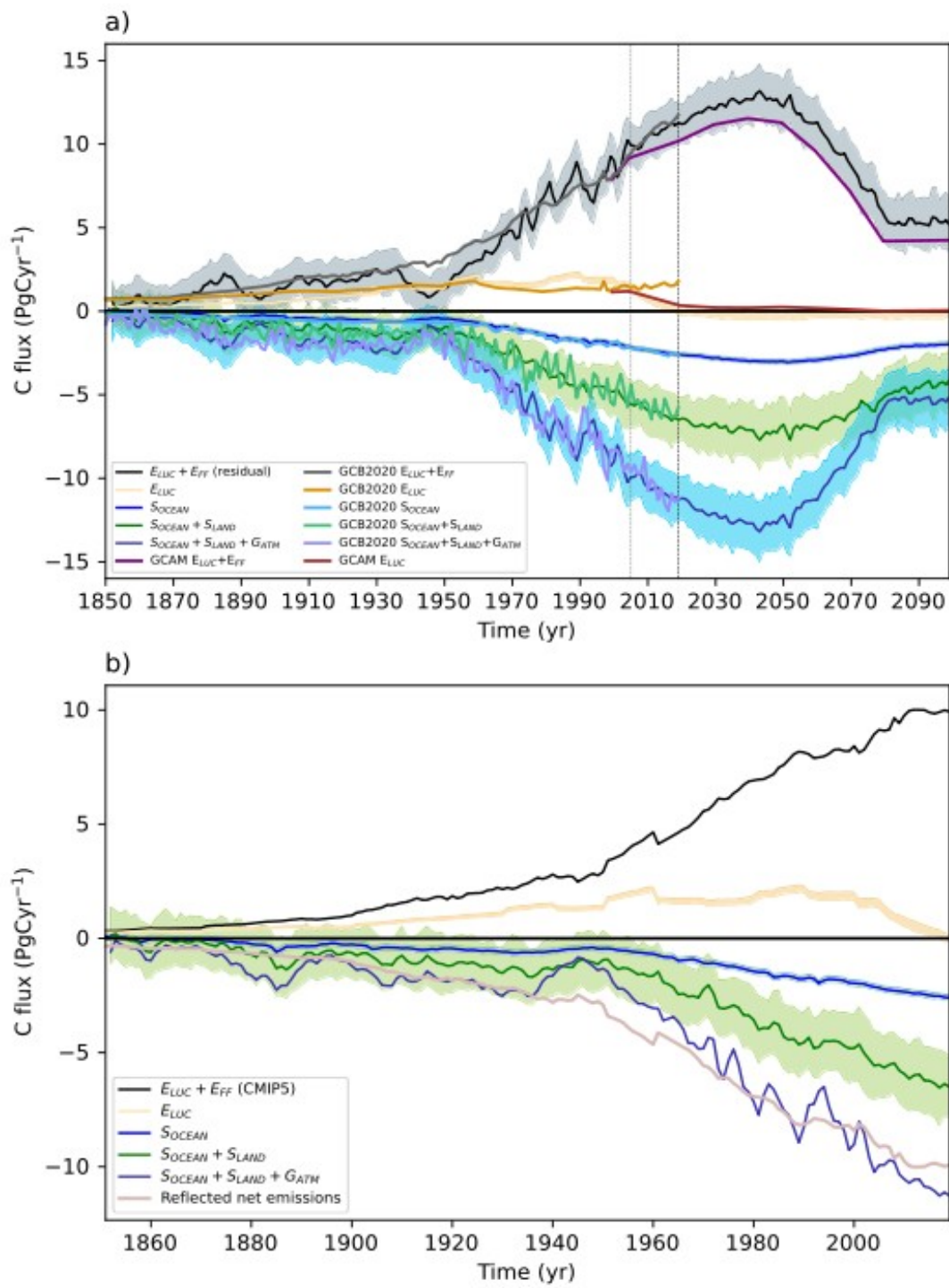


**Figure 2.** Stacked decomposition of the CO<sub>2</sub> budget terms from the MPI-GE for the historical (1850–2005) and RCP4.5 (2006–2099) scenarios (a) (unstacked plots of the individual terms can be found in Figure S1). Thick lines mark the ensemble mean and shading marks the range of the ensemble  $\pm 1$  standard deviation. Overlaid are the GCB2020 budget terms for comparison. Vertical lines mark the end of the historical period (2006) and the end of the latest GCP budget (2019). An alternative budget using the CMIP5  $E_{FF}$  taken from Andres et al. (2012) is also provided (b). The pink line shows the reflected net emissions, the difference with the net natural sinks would give the simulated  $B_{IM}$  term in Figure S1 f.

The budget terms in Figure 2 are stacked for  $S_{LAND}$  and  $G_{ATM}$ , and hence the shown standard deviation of the ensemble members for these terms aggregates according to a normal sum distribution (i.e.,  $\sigma(S_{OCEAN}+S_{LAND})=\sqrt{\sigma^2(S_{OCEAN}) + \sigma^2(S_{LAND})}$ ). The atmospheric concentration is prescribed to be the same for all ensemble members, and so  $G_{ATM}$  has no ensemble standard deviation. The standard deviation of residual  $E_{FF}$  is inherited directly from the net natural sinks and  $E_{LUC}$  because it is calculated as a residual in the budget.  $S_{OCEAN}$  has a stable standard deviation of  $\sim 0.15$  Pg C yr<sup>-1</sup> (Figure 3 c), which does not have a trend.  $S_{LAND}$  has the largest standard deviation throughout the historical period and the RCP4.5 scenario (see Figure 3 d), therefore the standard deviation of the net of natural sinks in Figure 2 (and consequently residual  $E_{FF}$ ) mostly originates from  $S_{LAND}$ . Standard deviation increases with time for residual  $E_{FF}$  and  $S_{LAND}$  (Figure 3 a & d) from  $\sim 1$  Pg C yr<sup>-1</sup> in 1850 to  $\sim 1.5$  Pg C yr<sup>-1</sup> in 2100.  $E_{LUC}$  standard deviation gradually increases from almost 0 to  $\sim 0.2$  Pg C yr<sup>-1</sup> by 2010 and later (Figure 3 b).

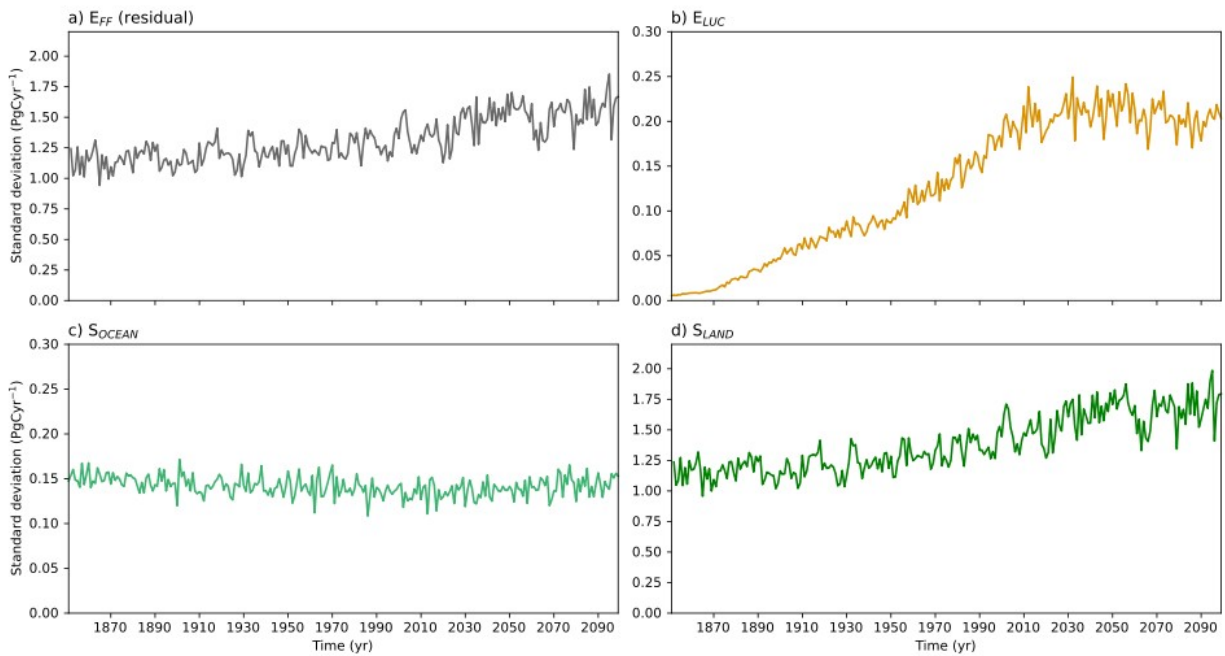


**Figure 3.** Yearly ensemble standard deviation for each carbon budget term. The emissions are on the top (a residual  $E_{FF}$  & b  $E_{LUC}$ ) and the natural sink terms are on the bottom (c  $S_{OCEAN}$  & d  $S_{LAND}$ ).

The importance of internal climate-driven variations (Figure 3) relative to the ensemble mean state can be better understood by analyzing the SNRs (Figure 4). Values greater than one indicate that the mean state dominates the signal, whereas values less than one indicate that the

internal climate variability uncertainty is the dominant factor in the carbon fluxes. For residual  $E_{FF}$  and  $S_{LAND}$  (Figure 4 a & d), internal variations are more relevant up until 1970. After that, the mean carbon fluxes (i.e. the forced signal) are much larger than the variations due to internal climate variability, for example  $\sim 2.5$ –3 times greater for  $S_{LAND}$ .  $S_{OCEAN}$  generally follows the same pattern (Figure 4 c); the internal climate variability remains several times smaller than the mean carbon flux to the ocean from about 1890 onward. On the other hand, the standard deviation in  $E_{LUC}$  is as large as the mean from 2010 onward (Figure 4 b), however, this is likely a consequence of the simulation setup: land-use changes begin in 1850 but the full range of variation from the legacy emissions of land-use change does not manifest until several decades later. This means the  $E_{LUC}$  SNR is effectively only valid under the future scenario when the mean  $E_{LUC}$  is small.

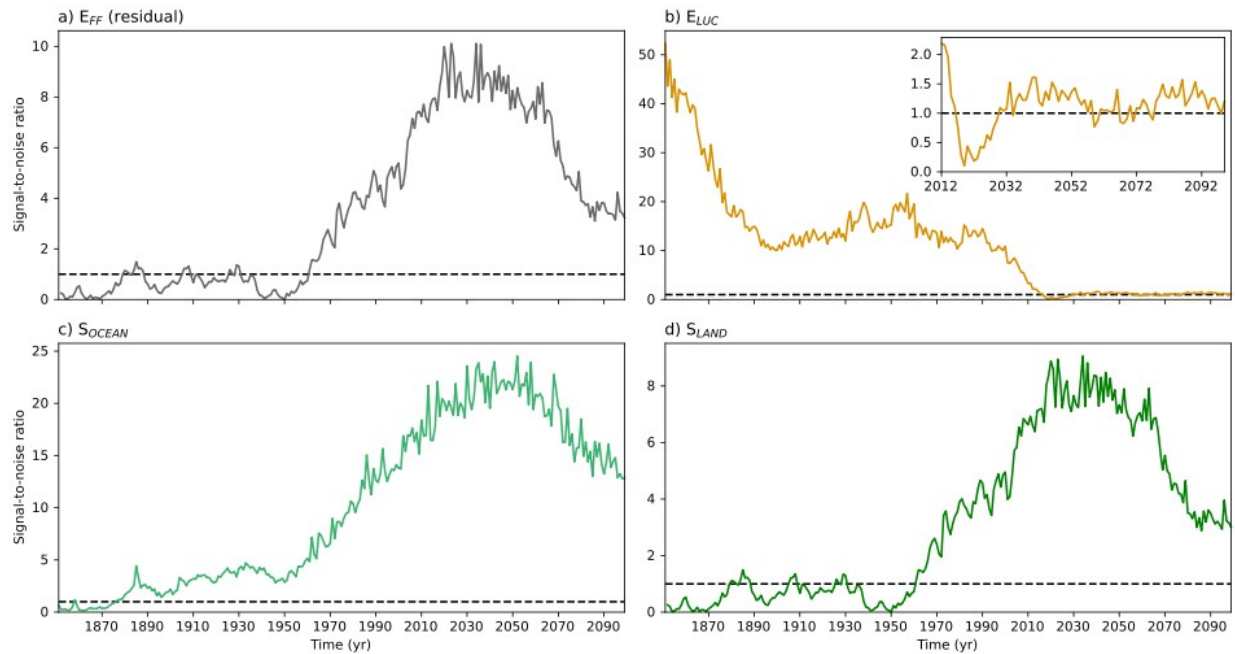


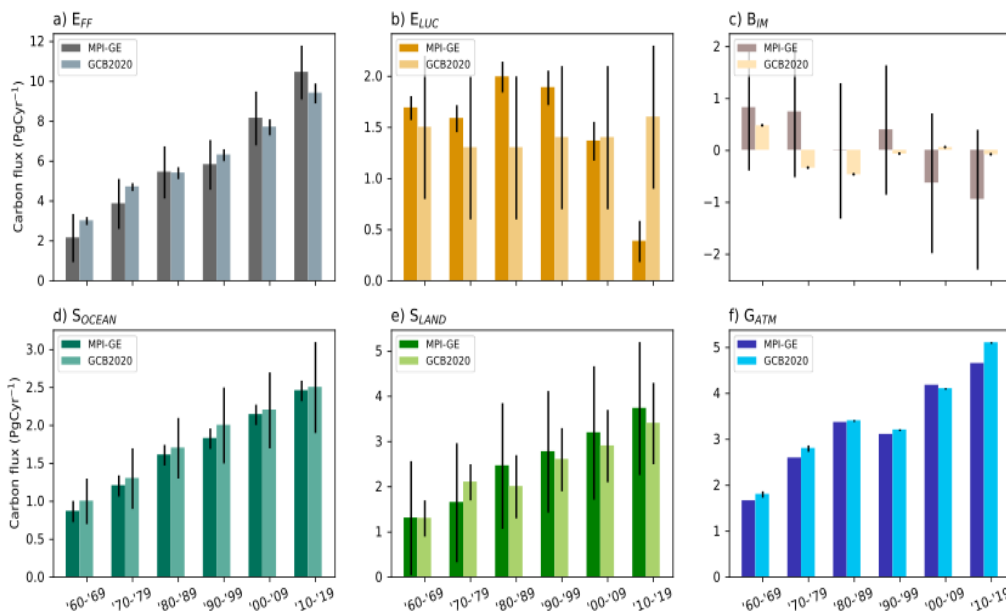
**Figure 4.** Yearly signal-to-noise ratio for each budget term in the MPI-GE. Dashed lines delineate ratio 1, where the standard deviation of the respective flux equals the mean flux.  $E_{LUC}$  has an inset plot with the post 2010 period zoomed in, when variations from legacy land-use fluxes have fully established.

### 3.2 Comparison to GCB2020

#### 3.2.1 Comparison of means

We compare here the GCB2020 mean of each budget term to the ensemble mean of the MPI-GE for each decade, before comparing the variances in the following sections. Firstly, the residual  $E_{FF}$  mean increases faster in the MPI-GE than observed in the GCB2020 (Figure 5 a). Initially, MPI-GE residual  $E_{FF}$  in the 1960s is less than the GCB2020 estimate by  $0.8 \text{ Pg C yr}^{-1}$  while it is greater than it by  $1.3 \text{ Pg C yr}^{-1}$  in the 2010–2018 decade. However, the range of GCB2020 means is well within the range of values simulated by the MPI-GE. Secondly, there are large differences in the mean  $E_{LUC}$  fluxes between MPI-GE and GCB2020 (Figure 5 b). MPI-GE  $E_{LUC}$  is larger compared to GCB2020 in decades prior to 2000, however, these values are also within the large

uncertainty ranges of the GCB2020. In recent decades, the MPI-GE estimates lower  $E_{LUC}$  than the GCB2020. Thirdly,  $S_{LAND}$  tends to be slightly higher in the MPI-GE for almost all decades (Figure 5 e). Fourthly,  $S_{OCEAN}$  mean fluxes in MPI-GE and GCB2020 are very similar (Figure 5 d). Lastly,  $G_{ATM}$  in MPI-GE has similar decadal variations as GCB2020, both displaying a dip in the 1990s, and there is no consistent bias (Figure 5 f).



349

**Figure 5.** Decadal average of carbon flux budget terms (bars), and the uncertainty expressed as  $\pm 1$  standard deviation from the mean (error whiskers). The MPI-GE uncertainties are ensemble standard deviations and the GCB2020 uncertainties are multi model standard deviations. The dark bars are the MPI-GE and the lighter bars are the GCB2020 values taken from Friedlingstein et al. (2019). The top row (a and b) are the emissions and the simulated budget imbalance term (c) as shown in Figure 2 b, and the bottom row (d, e and f) are the sink terms.

### 3.2.2 Un-bias-corrected comparison of uncertainties

The uncertainty ranges in Figure 5 are based on ensemble standard deviations for MPI-GE (and therefore reflect internal climate variability uncertainties) and multi-model standard deviation for GCB2020. These ranges can tell us two things: how realistic the MPI-GE range of fluxes is compared to observations, and how large uncertainties associated with internal climate variability are compared to other sources of uncertainty (e.g. from observational measurements or the differing process representations in the different GCB2020 models). Therefore, we will determine here whether the GCB2020 mean state lies outside the MPI-GE uncertainty ranges for each budget term.

Residual  $E_{FF}$ ,  $B_{IM}$  (based on the budget in Figure 2 b) and  $S_{LAND}$  (Figure 5 a, c & e) have larger standard deviations in the MPI-GE compared to GCB2020, i.e. internal variability is a larger source of error than observational and model uncertainty (more detail follows in 3.2.3). The GCB2020 mean for these budget terms falls within the MPI-GE uncertainty ranges for each budget term.

On the other hand,  $E_{LUC}$  and  $S_{OCEAN}$  have a narrower range of internal climate variability uncertainty in the MPI-GE compared to the modeled uncertainty in the GCB2020 (Figure 5 b & d). While the GCB2020 mean is within the MPI-GE uncertainty for  $S_{OCEAN}$  for most decades (indicating consistency between the two),  $E_{LUC}$  GCB2020 means are outside the corresponding MPI-GE ranges for nearly all decades. However, the uncertainty ranges of MPI-GE and GCB2020 overlap for both  $S_{OCEAN}$  and  $E_{LUC}$ , i.e. certain ensemble members match certain GCB2020 models. Only, the  $E_{LUC}$  2009–2018 mean and standard deviation of the GCB2020 is outside the standard deviation range of uncertainty due to internal climate variability, indicating clear inconsistency (see discussion section 4.1).

There is no uncertainty range for  $G_{ATM}$  from MPI-GE (Figure 5 f) since all ensemble members are prescribed with the same atmospheric  $CO_2$  concentration. The error whiskers in the  $G_{ATM}$  GCB2020 are derived from various observational uncertainties, which are very small compared to the terms that are simulated by dynamical models ( $S_{LAND}$ ,  $S_{OCEAN}$ , and  $E_{LUC}$ ). Because the MPI-GE  $CO_2$  concentration starting 2006 is derived from the Global Change Assessment Model (GCAM; Thomson et al. 2011), the difference in  $G_{ATM}$  between MPI-GE and the GCB2020 for the last two decades may in part be due to the differences in carbon cycle processes that are represented in MPI-ESM and GCAM.

### 3.2.3 Bias-corrected comparison of uncertainties

To more directly evaluate the magnitude of the historical uncertainties associated with internal climate variability compared to the GCB2020, Figure 6 shows the standard deviations where the biases in the means have been removed (centered). The models used in the GCB2020 estimates are forced by only one realization of the climate state—the actual historical climate evolution. Therefore, the plausible carbon fluxes under different climate states cannot be inferred using only the GCB2020, and while the models used in the GCB2020 do contain internal climate variability, the multi-model standard deviations only account for model uncertainty, but not that from natural variability. If we assume that there is no or negligible uncertainty due to internal climate variability associated with the multi-model GCB2020 standard deviation and that the standard deviation of the MPI-GE is entirely due to internal climate variability, then we can find the proportion of the total uncertainty attributable to internal climate variability (i.e. the sum of GCB2020 and MPI-GE uncertainties; red lines in Figure 6). The importance of internal climate variability decreases with time for  $S_{LAND}$  and residual  $E_{FF}$  and the MPI-GE land sink uncertainty increases faster than the multi-model uncertainty in the GCB2020. For the 2009–2018 decade the contribution of internal climate variability to total uncertainty is 70% for the residual  $E_{FF}$  and 60% for  $S_{LAND}$ . A constant multi-model uncertainty was assumed for  $E_{LUC}$  in the GCB2020 and therefore the MPI-GE  $E_{LUC}$  uncertainty increases gradually relative to it. By the 2009–2018 decade the uncertainty due to internal climate variability would account for 22% of the total  $E_{LUC}$  uncertainty. Lastly, approximately 20% of total uncertainty is from internal climate variability uncertainty for  $S_{OCEAN}$ .



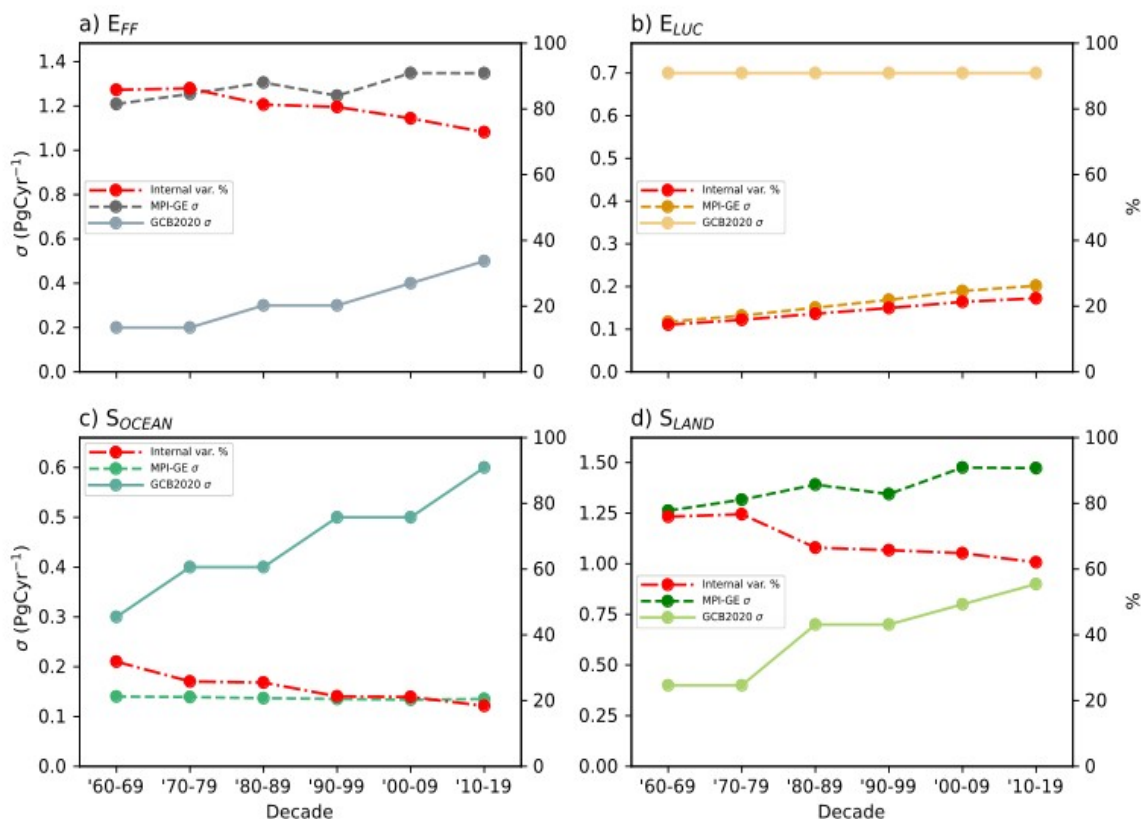


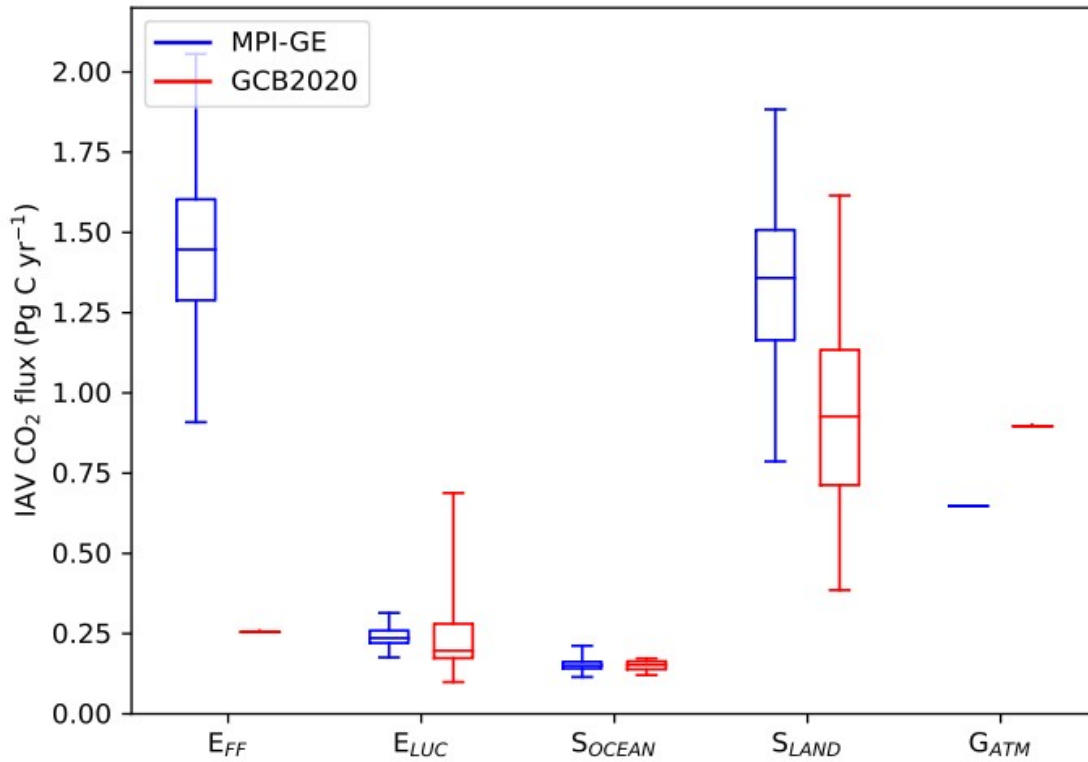
**Figure 6.** Centered standard deviation of carbon flux from the multi-model GCB2020 (solid lines) and ensemble standard deviation from the MPI-GE (dashed lines). The relative contribution of internal climate variability uncertainty is marked in red (dot-dashed lines corresponding to the right-hand axis). The color coding is the same as that used in Figures 2–5.

### 3.2.4 Interannual variability

The ability of individual ensemble members to capture the IAV (in the base period 1961–1990) for each term compared to the GCB2020 IAVs is shown in Figure 7. The ranges of the IAVs generally have good overlap for the  $E_{LUC}$  and  $S_{OCEAN}$  budget terms. This means that individual MPI-GE members can simulate a plausible range of IAV values that are not significantly different from the published values from the GCB2020.  $S_{LAND}$ , however, shows some IAV bias in the MPI-ESM compared to other models in the GCB2020. IAV in MPI-GE  $S_{LAND}$  tends to be on average 0.4 Pg C yr<sup>-1</sup> larger than other models. A higher IAV may contribute to the large ensemble spread in the MPI-GE for  $S_{LAND}$  (compare to Figure 5). There are large differences between MPI-GE and GCB2020 for  $E_{FF}$ , and  $G_{ATM}$  (Figure 7). Evaluation of  $G_{ATM}$  is difficult because there is no associated uncertainty range; the GCB2020 only has one potential realization of past emissions and observed CO<sub>2</sub> concentration, and the MPI-GE atmospheric CO<sub>2</sub> concentrations are prescribed. The observationally-based GCB2020 uncertainties are only 0.02



426 Pg C yr<sup>-1</sup> for  $G_{\text{ATM}}$  and at most 0.5 Pg C yr<sup>-1</sup> for residual  $E_{\text{FF}}$  and if we use these values as a range  
 427 on top of the GCB2020 IAV, MPI-GE is still outside these ranges.



428

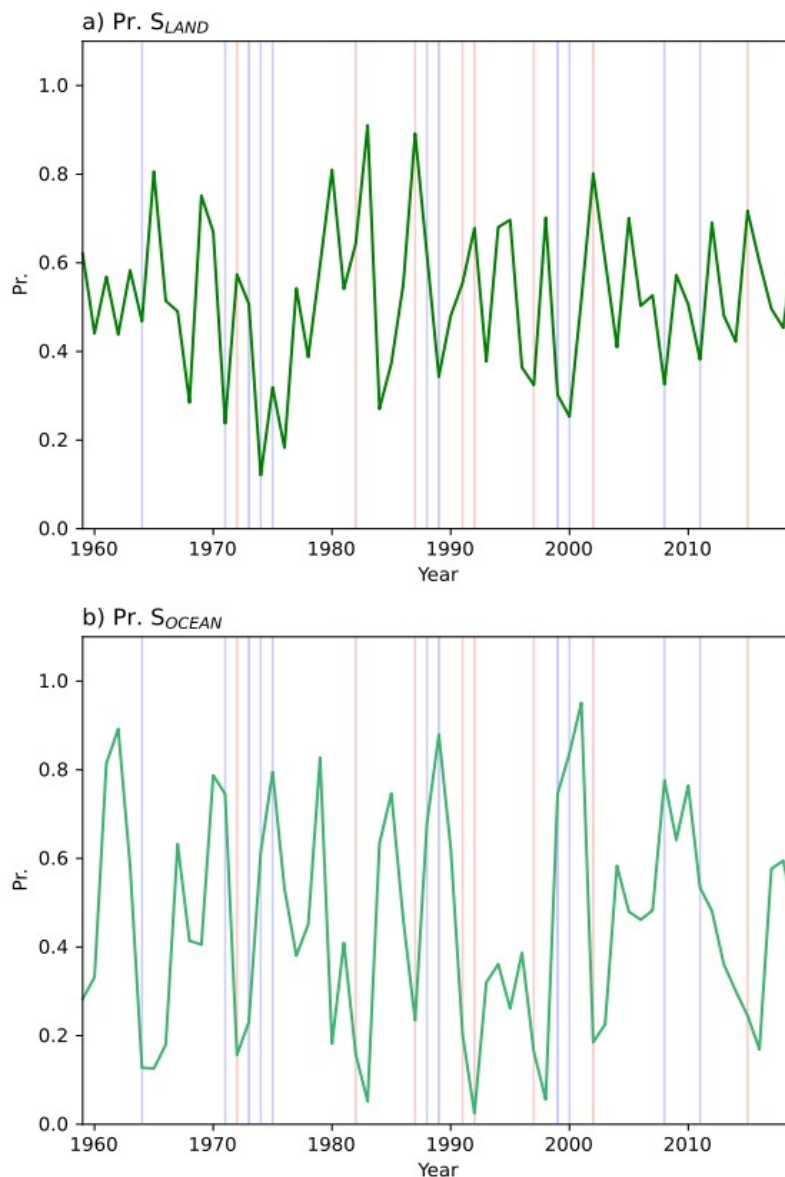
429 **Figure 7.** Box and whisker plots of interannual variability (IAV) calculated as the standard  
 430 deviation over the base period 1961–1990 for the MPI-GE (blue) and the GCB2020 (red). The  
 431 ranges shown here are derived from the ensemble members for MPI-GE, and from multiple  
 432 model simulations for the GCB2020. The boxes mark the median and inter-quartile range, and  
 433 the whiskers mark the full range of values.

### 434 3.3 The relationship of historical probabilities to ENSO

435 To investigate a potential source of the IAV and uncertainty from internal climate variability, we  
 436 examine here the exceedance probabilities and the relationship to ENSO. Figure 8 shows the  
 437 probability of the magnitude of the past carbon fluxes in GCB2020 with respect to the  
 438 distribution of the MPI-GE. Higher values indicate years where the carbon flux for the respective  
 439 sink was unusually small compared to the MPI-GE distribution and thus were more likely to be  
 440 exceeded under more favorable climate conditions.  $S_{\text{LAND}}$  and  $S_{\text{OCEAN}}$  have large annual variations  
 441 in exceedance probability. For example, since 1960 there were three years where the historical  
 442  $S_{\text{LAND}}$  was so high, related to La Niña, that it had a chance of less than 20% to be exceeded and  
 443 five years with  $S_{\text{LAND}}$  so low that it had a chance of more than 80% to be exceeded (Figure 8 a).  
 444 This highlights the importance of using a large ensemble to capture the high variability in  $S_{\text{LAND}}$   
 445 (see Section 4.5). The cause of these year-to-year variations may come from a variety of internal  
 446 climate variability modes. To investigate potential drivers, Figure 9 shows that there are

447 significant correlations between the Niño 3.4 index and  $S_{OCEAN}$  or  $S_{LAND}$  exceedance probability of  
 448 -0.61 and 0.56 respectively (see also Supplementary Text and Figure S2).

449



450 **Figure 8.** Probability of exceedance that the MPI-GE carbon fluxes are greater than the historical  
 451 GCB2020 mean. Lower values indicate years where the carbon flux to the respective sink was  
 452 *unusually* high compared to the MPI-GE *distribution* (*vice versa* for *large values*). The vertical  
 453 lines mark El Niño (red) and La Niña (blue) years where Niño 3.4 index is greater than 1  
 454 standard deviation from the mean.

455

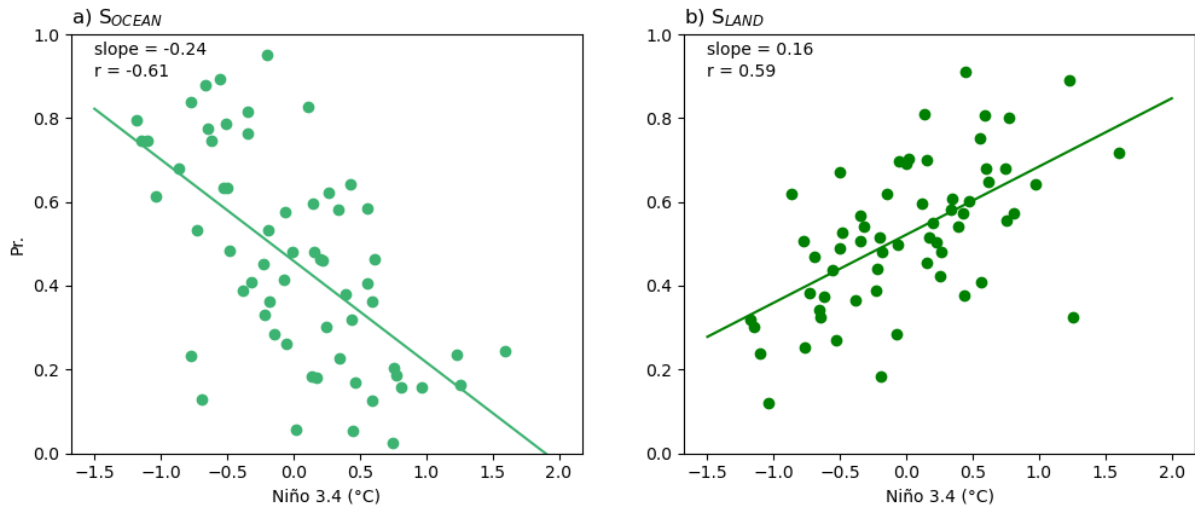


**Figure 9.** Regression and correlation analysis between Niño 3.4 index and the probability of exceedance for carbon fluxes a)  $S_{OCEAN}$  and b)  $S_{LAND}$ . The units of the slope are in  $^{\circ}\text{C}^{-1}$ .

#### 4 Discussion

In summary,  $S_{LAND}$  has the largest uncertainty, which emphasizes the dominant role of internal climate variability on the land sink (Figure 3 d). This uncertainty gradually increases over time to approximately  $\pm 1.5 \text{ Pg C yr}^{-1}$ . While the global  $S_{LAND}$  flux and  $\text{CO}_2$  concentration increases until the middle of the 21<sup>st</sup> century (Figure 2), afterwards its signal-to-noise ratio of the mean flux nevertheless decreases (Figure 4 b). The internal climate variability uncertainty in  $E_{LUC}$  is relatively smaller at approximately  $\pm 0.2 \text{ Pg C yr}^{-1}$  (Figure 3 b). However, the trend in  $E_{LUC}$  variability is likely due to a combination of sensitivity to initial conditions and the time delay associated with legacy land-use change emissions. The  $S_{OCEAN}$  variations from internal climate variability are similarly small as those in  $E_{LUC}$  but show almost no trend (Figure 3 c). The  $S_{LAND}$  internal climate variability accounts for about 70% of the total uncertainty that results from both internal variability and uncertainties from models and observations (Figure 6 d), much more than for  $E_{LUC}$  (approximately 22%) and  $S_{OCEAN}$  (approximately 19%). The standard deviations of the MPI-GE compare well with the uncertainty ranges of the GCB2020 for most budget terms: with respect to the ensemble standard deviation against multi-model standard deviations (usually at least an overlap, Figure 5), and with respect to individual ensemble IAV against individual model IAV in the GCB2020 (Figure 7). Finally, we show that the effect of internal climate variability on the historically observed exceedance probabilities of carbon fluxes to the land and ocean have significant but moderate correlations to ENSO (Figure 9).

##### 4.1 Differences between MPI-GE and GCB2020

One of the most striking differences between the MPI-GE and the GCB2020 estimates is in  $E_{LUC}$ , where the forced ensemble mean signal from land-use change in the RCP4.5 scenario differs from the observed LUH2 data in the last historical decade. The MPI-GE  $E_{LUC}$  transitions to a net sink at around 2020, while the forcing used in GCB2020 estimates sustained  $E_{LUC}$  until this period (Friedlingstein et al. 2020, Bastos et al. 2020). Given that the variance of  $E_{LUC}$  ensemble

members is quite small compared to the forced mean response, the disparity between the RCP4.5 land-use change and the GCB2020 becomes evident. The RCP4.5 scenario is characterized by a high CO<sub>2</sub> price that encourages investment into agricultural intensification rather than expansion. Consequently, re-/afforestation would occur following widespread abandonment of agricultural lands and substantial deforestation reduction since 2007 (Thomson et al. 2011). Despite the process of forest regrowth (such as that in North America and Europe; Doelman et al. 2020) being slow, the MPI-GE reduction in  $E_{LUC}$  associated with stopping deforestation globally (in particular the Amazon and other tropical regions) is quick and modeling studies simulate substantial carbon uptake by re-/afforestation and reduced deforestation. For example, Sonntag et al. (2016) estimate an uptake of about 200 Pg C over the 21st century with RCP4.5 land-use change in an RCP8.5 climate compared to unmitigated deforestation. However, the trajectory of RCP4.5 land-use change has not been followed until now, and so the land-use-related mitigation potential remains untapped. This explains the large divergence of our results from the GCB2020 estimates for the last 15 years.

There are also considerable differences in the “compatible” residual  $E_{FF}$  in the MPI-GE compared to the GCB2020 values. If we assume the GCB2020 estimate to be the closest estimate to the mean in reality, then the MPI-GE first underestimates the  $E_{FF}$  then overestimates it. The discrepancy may arise due to the closure of the carbon balance and the consequent effect that  $S_{LAND}$  has on the compatible emissions. On the other hand, the GCB2020 has an imbalance term that includes carbon fluxes that remain unaccounted for. This term would include errors introduced by the calculation of budget terms independently (e.g. model bias errors in  $E_{LUC}$  and  $S_{LAND}$ , e.g. Dai and Fung, 1993), errors from incomplete coverage of observations, and minor terms that are not included in the budget decomposition. For these reasons, we would not expect the MPI-GE to accurately reproduce  $E_{FF}$ .

Lastly, another approach to evaluating the MPI-GE against the GCB2020 is to verify that there are no trends in the budget imbalance relative to the GCB2020. If the compatible residual  $E_{FF}$  in the MPI-GE budget is replaced with the CMIP5  $E_{FF}$  values (Figure 2b), a budget imbalance term ( $B_{IM}$ ) can be calculated that is the residual carbon flux that is not accounted for under each ensemble member’s climate state. This simulated  $B_{IM}$  term (Figure S1 f) derived from the MPI-GE is largely consistent with the  $B_{IM}$  from the GCB2020 and shows no significant long-term trends over the analysis period. Both MPI-GE and GCB2020 show as a positive  $B_{IM}$  around the 1950s and again more briefly in the 1990s (suggesting either an overestimate in the emissions or underestimate in the sinks). While Friedlingstein et al. (2020) could not directly attribute a cause to the  $B_{IM}$ , they suggest that its variations originate mostly from  $S_{LAND}$  and  $S_{OCEAN}$ . Specifically, they suggest that it could originate from internal variability which models cannot capture with a single realization. However, the multiple realizations in the MPI-GE  $B_{IM}$  range also show positive values in the 1950’s, which suggests that it is more likely from common deficiencies in model physics, resolution, or forcing data. In particular, the land-use forcing could explain the 1950s  $B_{IM}$ , as the LUH2 forcing creates large emissions in the 1950s (e.g., Hansis et al. 2015) not captured by datasets based on other land-use forcing such as FAO (Houghton and Nassikas 2017).

## 4.2 Allowable emissions under RCP4.5

The standard deviations in the MPI-GE (Figure 2) are derived either directly from the ensembles or are inferred from other budget terms, and therefore they should be interpreted with care. The

standard deviation of residual  $E_{FF}$  is mostly derived from  $S_{LAND}$  due to its calculation as a residual. In this case, the ranges here are merely a range of emissions that are compatible with the likely range of climate states, and the corresponding strengths of the ocean and land sinks. Therefore, the residual  $E_{FF}$  uncertainty estimates from MPI-GE should not be interpreted as variations in fossil fuel emissions due to internal climate variability-related global demand.

The net sinks and the corresponding compatible residual  $E_{FF}$  range are still useful when deciding what the allowable future emissions may be. They indicate the allowable emissions (accounting for internal climate variability) if appropriate policies are implemented to successfully mitigate climate change in a manner that is consistent with the RCP4.5 scenario. Therefore, the maximum and minimum ensemble ranges of 9–18 Pg C yr<sup>-1</sup> in residual  $E_{FF}$  at 2050 denote allowable emissions under this scenario (2019 was 9.95 Pg C yr<sup>-1</sup> as per the GCB2020). In Fig 2 the  $\pm 1$  standard deviation range of the ensemble is shown instead. In the comparison it is clear that extreme outliers occur mainly at the maximum end. These maximum values may occur before fossil emissions have to drop steeply in the MPI-GE and level off at around 5 Pg C yr<sup>-1</sup> if the 3°C target is to be met by 2100. This evolution matches well the fossil emissions estimates from GCAM (Thomson et al. 2011) but allows some higher peak emissions than the Integrated Assessment Model assumed, suggesting smaller assumed sinks and slightly larger  $E_{LUC}$  in the simplified carbon cycle of this assessment model (see Figure 2 to compare to  $E_{FF}$  and  $E_{LUC}$  from GCAM).

As highlighted by Mankin et al. (2020), decision makers need to be provided the full range of possible outcomes in order to make appropriate decisions. For example, policy decisions based only on the most likely outcome may lead to a blowout of greenhouse gas inventory targets, particularly if  $S_{LAND}$  performs poorly within a given 5-year accounting period of the Paris Agreement's Global Stocktake (UNFCCC, 2015 and 2017). On the other hand, caution should be taken when considering the efficacy of past decision making because internal variability uncertainties can potentially obfuscate emission reduction efforts such as re-/afforestation.

#### 4.3 Trends in uncertainty

The increase in standard deviation in the ensemble members for  $S_{LAND}$  may be due to an increase in the variability in the climate state as is expected under a warming climate. For example, Maher et al. (2019) find an increase in the global mean precipitation variability in the MPI-GE 1% CO<sub>2</sub> scenario. The trend in  $S_{LAND}$  internal variability can also potentially arise from the increase in the magnitude of fossil emissions, which is initially forced in the MPI-GE as the prescribed atmospheric CO<sub>2</sub> concentration. Larger emissions would result in higher atmospheric CO<sub>2</sub> concentrations and increased potential carbon uptake by vegetation via so-called CO<sub>2</sub> fertilization (Walker et al. 2021). This combined with the effect of unfavorable climatic conditions (i.e. heat and drought stress) on the carbon uptake by plants acting on an increased carbon stock, results in a larger variance depending on the climate conditions. The increasing internal variability makes it more likely that  $S_{LAND}$  becomes near-neutral by the end of the century compared to the start of the historical period (Figure S1 d). This contrasts somewhat with  $S_{OCEAN}$ , which has a relatively lower variance and does not have a trend in the historical or future periods under the RCP4.5 scenario (a similar standard deviation is found by Li and Ilyina 2018). However, under higher emissions scenarios  $S_{OCEAN}$  has been shown to also have increasing trends in CO<sub>2</sub> flux standard deviation (see Figure 1 of Maher et al. 2019).

The trend in  $E_{LUC}$  may arise for several reasons. Firstly, the legacy effects of land-use change (mostly from wood harvest) take time to manifest. The anthropogenic pools in which CBALONE stores deforested biomass decay to the atmosphere at time scales of 1–100 years. The variance of the ensemble members therefore not only depends on the climate variability of the current year but also on that of preceding years. Consequently, it would take at least 100 years for the full variance due to land-use change to manifest. Similarly, the carbon pool of woody, slowly-decomposing litter left on site after clearing or harvesting will build up over time as land-use transitions occur. Thus, more litter is available to react to the climate-dependent microbial decomposition. Note that while the study of Yue et al. (2020) included this effect in their assessment of the contribution of land-use to the interannual variability of the land carbon pools, their high IAV of  $E_{LUC}$  (30–45% of net land exchange IAV, compared to 15% in this study) also originates from attributing part of  $S_{LAND}$  (the part on managed land) to  $E_{LUC}$ . Internal variability alone, our study shows, is about 0.25 Pg C yr<sup>-1</sup> standard deviation for  $E_{LUC}$  in recent decades (Figure 3) or 20% of the total uncertainty (model plus internal; Figure 6). IAV of  $E_{LUC}$  in the MPI-GE is only slightly larger than in the GCB2020 (Figure 7), indicating that the main driver is not internal climate variability, but land-use forcing.

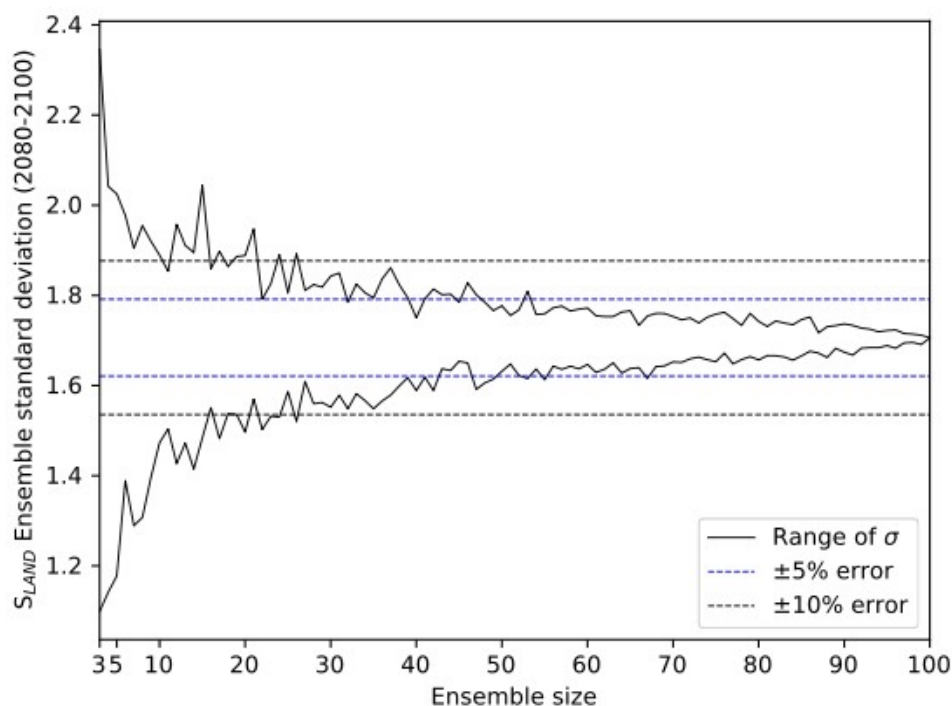


**Figure 10.** Range of ensemble standard deviation (2080–2100) as a function of sample size from 30 sub-samples for  $S_{LAND}$ .

While the data analyzed in this study is annual and much of the analysis concerns interannual variations, we conducted simulations for several centuries, and therefore the longer time scale variations must also be considered. There are centennial-scale internal variations in the land carbon content in JSBACH3 and CBALONE (see Figure 2 in Schneck et al. 2013)

which could influence trends and variability of  $S_{\text{LAND}}$  and  $E_{\text{LUC}}$  for simulations that run for several hundred years. These variations have a periodicity of  $\sim 250$  years and consist of a change in the total land carbon content of  $\sim 8 \text{ Pg C}$ . This corresponds to an average land carbon flux of  $0.03 \text{ Pg C yr}^{-1}$  or roughly 2% of the MPI-GE  $S_{\text{LAND}}$  standard deviation. Schneck et al. (2013) suggest that these long-duration variations in land carbon content are linked to variations in anthropogenic land cover changes, and the modulation of soil respiration by long-term changes in temperature from volcanism and solar forcing. Since the duration of the MPI-GE and CBALONE simulation in this study is 250 years, it is possible that these long-term variations may affect the estimates of internal climate variability uncertainty in  $S_{\text{LAND}}$ .

#### 4.4 ENSO as a potential source of variability

ENSO is positively correlated with  $S_{\text{LAND}}$  exceedance probabilities and negatively correlated with  $S_{\text{OCEAN}}$  exceedance probabilities, which is consistent with how ENSO affects  $\text{CO}_2$  fluxes to the land surface and ocean. During La Niña, cool and moist mean global conditions tend to encourage vegetative productivity on land and increase land carbon storage, while El Niño drought conditions put widespread stress on ecosystems and suppress productivity (Gonsamo et al. 2016; Jones et al. 2001). Meanwhile, over the ocean, stronger Pacific equatorial up-welling during La Niña brings dissolved inorganic carbon-rich subsurface water to the surface, thereby favoring  $\text{CO}_2$  out-gassing and reducing net  $\text{CO}_2$  uptake (Jones et al. 2001; Feely et al. 1999). The cooler sea surface temperatures during La Niña events can increase the dissolution of  $\text{CO}_2$  and can reduce  $\text{CO}_2$  outgassing, but this is a smaller term relative to the up-welling-induced  $\text{CO}_2$  outgassing. This could explain the diverging response of  $S_{\text{OCEAN}}$  to ENSO compared to that of  $S_{\text{LAND}}$ . The moderate correlation suggests that while ENSO may have a considerable impact on interannual variations in  $\text{CO}_2$  fluxes, it is very likely that other climate modes and internal dynamics are also important. No significant correlations with other climate modes could be found at the global scale, however the impacts of climate modes on regional budgets may be considerable.

#### 4.5 Importance of ensemble size

Lastly, it is important to discuss the effect of ensemble size on the results and whether or not using 100 members is enough or more than necessary. A framework to assess this is demonstrated in Milinski et al. (2020). In accordance with this framework, our goal is to quantify variability using the metric of ensemble standard deviation, to within 5% accuracy of the full 100 member variance. We estimate standard deviation using 30 iterations of subsample sizes from 3–100 members without replacement. Figure 10 suggests that at least 40 ensemble members are required to capture the standard deviation of  $S_{\text{LAND}}$  to within  $\pm 5\%$  accuracy. Since  $S_{\text{LAND}}$  has the largest standard deviation of all budget terms, the accuracy of a sub-sample of the carbon budget decomposition would depend on this term. The other budget terms (Figure S5) do not display variations as large as  $S_{\text{LAND}}$  and therefore 40 members are sufficient for those terms. Whether this result is representative of other models that simulate internal variability through ensemble simulations depends on the budget terms. In the absence of extensive multi-model large ensemble projects that provide the full suite of budget terms, including the split into  $S_{\text{LAND}}$  and  $E_{\text{LUC}}$ , we evaluated this based on the IAV in the models participating in the GCB2020 simulations that are forced with observed climate (Figure 7). A key assumption is that MPI-GE is capable of accurately representing IAV, and the fact that MPI-GE slightly overestimates  $S_{\text{LAND}}$

IAV by  $0.4 \text{ Pg C yr}^{-1}$  compared to other models in the GCB2020 suggests that the minimum 40 ensemble members required here may be a conservative estimate.

## 5 Conclusion

In this study, we use a large ensemble of single-model simulations from the Max Planck Institute Grand Ensemble and a sub-component of JSBACH3 (called CBALONE) to decompose the global anthropogenic carbon budget into fossil and land-use change emissions, atmospheric growth, and natural land and ocean sinks. Through its 100 ensemble members, the MPI-GE captures the uncertainties associated with internal climate variability, which we compare to the 2020 global carbon budget's uncertainty and interannual variability, and calculate exceedance probabilities of the past carbon fluxes with respect to a full range of climate variability states. We estimate about 40 ensemble members are required to capture internal variability in  $S_{\text{LAND}}$  and thus all budget components. Contrary to  $S_{\text{LAND}}$ , to reduce uncertainty in  $S_{\text{OCEAN}}$  and  $E_{\text{LUC}}$  estimates, we must prioritize reducing observational error and model spread rather than capturing internal variability. Despite its high internal variability,  $S_{\text{LAND}}$  (or  $S_{\text{OCEAN}}$ ) is likely not the reason behind the high budget imbalance found in previous studies for the 1950s, which suggests common model deficiencies or biases in the land-use forcing.

We also present a novel estimate of the uncertainty in land-use change emissions associated with internal climate variability at approximately  $\pm 0.2 \text{ Pg C yr}^{-1}$ , which we estimate would account for about 20% of the total (internal and multi-model) land-use change emissions uncertainties. Land-use change emissions thus contribute little to interannual variability of the annual carbon budget and are driven rather by land-use forcing than by climate variability.

We investigate future changes in the global carbon budget under RCP4.5 and demonstrate upper and lower bounds on the allowable future  $\text{CO}_2$  emissions depending on climate variations. The RCP4.5 scenario exemplifies a future where climate policies are implemented to limit warming to less than  $3^\circ\text{C}$  over present-day conditions. Our study largely confirms that the allowable emissions under the assumptions of the socioeconomic model GCAM are compatible with RCP4.5, though slightly higher emissions of up to  $13 \text{ Pg C yr}^{-1}$  on average would be allowed in the MPI-ESM. The minimum of the full ensemble range is  $9 \text{ Pg C yr}^{-1}$  and would be the lower risk limit to ensure we stay below  $3^\circ\text{C}$  warming for all possible climate states, while the maximum of  $18 \text{ Pg C yr}^{-1}$  would be the higher risk limit for the climate states leading to stronger land  $\text{CO}_2$  uptake. Our results suggest that internal variability of the natural land sink increases over the 21st century, which puts the steady persistence of carbon removal by land ecosystems at risk. We also show that even when accounting for random variations in climate and natural sinks, the emissions in recent decades for land-use change—characterized by continuing global deforestation—are dangerously inconsistent with the RCP4.5 goals and further erode our ability to successfully mitigate future warming.

## Acknowledgments

The authors would like to acknowledge the generous help and comments from the Max Planck Institute Grand Ensemble working group. We also thank the German Climate Computing Centre (DKRZ), for providing computational resources. CMIP5 emissions data are available from RCP Database <http://www.iiasa.ac.at/web-apps/tnt/RcpDb> and the GCP Global Carbon Budgets data are available from <https://www.globalcarbonproject.org/carbonbudget/archive.htm>. H.L. was



supported by the European Union's Horizon 2020 research and innovation program under grant agreement no. 821003 (4C).

## References

- Andres, R. J., et al. (2012), A synthesis of carbon dioxide emissions from fossil-fuel combustion. *Biogeosciences*, **9**, 1845–1871, doi:[10.5194/bg-9-1845-2012](https://doi.org/10.5194/bg-9-1845-2012).
- Ballantyne, A. P., C. B. Alden, J. B. Miller, P. P. Tans, and W. C. White, (2012), Increase in observed net carbon dioxide uptake by land and oceans during the past 50 years. *Nature*, **488**, 70–72, doi:[10.1038/nature11299](https://doi.org/10.1038/nature11299).
- Bastos, A., S. W. Running, C. Gouveia, and R. M. Trigo (2013), The global NPP dependence on ENSO: La Niña and the extraordinary year of 2011: GLOBAL NPP AND ENSO: THE 2011 LA NIÑA. *Journal of Geophysical Research: Biogeosciences*, **118**, 1247–1255, doi:[10.1002/jgrg.20100](https://doi.org/10.1002/jgrg.20100).
- Bastos, A., et al. (2018), Impact of the 2015/2016 El Niño on the terrestrial carbon cycle constrained by bottom-up and top-down approaches. *Philosophical Transactions of the Royal Society B Biological Sciences*, **373**, 20170304, doi:[10.1098/rstb.2017.0304](https://doi.org/10.1098/rstb.2017.0304).
- Canadell, J. G. et al. (2007), Contributions to accelerating atmospheric CO<sub>2</sub> growth from economic activity, carbon intensity, and efficiency of natural sinks. *Proceedings of the National Academy of Sciences* **104**, 18866–18870, doi:[10.1073/pnas.0702737104](https://doi.org/10.1073/pnas.0702737104).
- Climate Prediction Center (2017), *Monthly Atmospheric SST Indices*, <https://www.cpc.ncep.noaa.gov/data/indices/>.
- Conway, T. J., P. P. Tans, L. S. Waterman, K. W. Thoning, D. R. Kitzis, K. A. Masarie, and N. Zhang, 1994: Evidence for interannual variability of the carbon cycle from the National Oceanic and Atmospheric Administration/Climate Monitoring and Diagnostics Laboratory Global Air Sampling Network. *Journal Geophysical Research Atmospheres*, **99**, 22831–22855, doi:[10.1029/94JD01951](https://doi.org/10.1029/94JD01951).
- Dai, A. and Fung, I. Y. (1993), Can climate variability contribute to the ‘Missing’ CO<sub>2</sub> sink? *Global Biogeochemical Cycles* **7**, 599–609, doi:[10.1029/93GB01165](https://doi.org/10.1029/93GB01165).
- Dannenberg, M. P., C. Song, T. Hwang, and E. K. Wise (2015), Empirical evidence of El Niño–Southern Oscillation influence on land surface phenology and productivity in the western United States. *Remote Sensing Environment*, **159**, 167–180, doi:[10.1016/j.rse.2014.11.026](https://doi.org/10.1016/j.rse.2014.11.026).
- Deser, C., Phillips, A., Bourdette, V. and Teng, H., (2012), Uncertainty in climate change projections: the role of internal variability. *Climate Dynamics* **38**, 527–546, doi:[10.1007/s00382-010-0977-x](https://doi.org/10.1007/s00382-010-0977-x).
- Dlugokencky, E., and P. Tans (2018), *Trends in atmospheric carbon dioxide*, National Oceanic & Atmospheric Administration, Earth System Research Laboratory (NOAA/ESRL).
- Doelman, J. C., et al. (2020), Afforestation for climate change mitigation: Potentials, risks and trade-offs. *Global Change Biology*, **26**, 1576–1591, doi:[10.1111/gcb.14887](https://doi.org/10.1111/gcb.14887).

- Feely, R. A., R. Wanninkhof, T. Takahashi, and P. Tans (1999), Influence of El Niño on the equatorial Pacific contribution to atmospheric CO<sub>2</sub> accumulation. *Nature* **398**, 597–601, doi:[10.1038/19273](https://doi.org/10.1038/19273).
- Friedlingstein, P., et al. (2019), Global Carbon Budget 2019. *Earth System Science Data*, **11**, 1783–1838, doi:[10.5194/essd-11-1783-2019](https://doi.org/10.5194/essd-11-1783-2019).
- Giorgetta, M. A., et al. (2013), Climate and carbon cycle changes from 1850 to 2100 in MPI-ESM simulations for the Coupled Model Intercomparison Project phase 5. *Journal of Advances in Modeling Earth Systems*, **5**, 572–597, doi:[10.1002/jame.20038](https://doi.org/10.1002/jame.20038).
- Goll, D. S. et al. (2015), Strong dependence of CO<sub>2</sub> emissions from anthropogenic land cover change on initial land cover and soil carbon parametrization. *Global Biogeochemical Cycles*, **29**, 1511–1523, doi:[10.1002/2014GB004988](https://doi.org/10.1002/2014GB004988).
- Gonsamo, A., J. M. Chen, and D. Lombardozzi (2016), Global vegetation productivity response to climatic oscillations during the satellite era. *Global Change Biology*, **22**, 3414–3426, <https://doi.org/10.1111/gcb.13258>.
- Hansis, E., S. J. Davis, and J. Pongratz (2015), Relevance of methodological choices for accounting of land use change carbon fluxes. *Global Biogeochemical Cycles*, **29**, 1230–1246, doi:[10.1002/2014GB004997](https://doi.org/10.1002/2014GB004997).
- Houghton, R. A., and A. A. Nassikas (2017), Global and regional fluxes of carbon from land use and land cover change 1850-2015: Carbon Emissions From Land Use. *Global Biogeochemical Cycles*, **31**, 456–472, doi:[10.1002/2016GB005546](https://doi.org/10.1002/2016GB005546).
- Huang, B., et al. (2017), Extended Reconstructed Sea Surface Temperature, Version 5 (ERSSTv5): Upgrades, Validations, and Intercomparisons. *Journal of Climate*, **30**, 8179–8205, doi:[10.1175/JCLI-D-16-0836](https://doi.org/10.1175/JCLI-D-16-0836).
- Hurt, G. C., et al. (2011), Harmonization of land-use scenarios for the period 1500-2100: 600 years of global gridded annual land-use transitions, wood harvest, and resulting secondary lands. *Climate Change*, **109**, 117–161, doi:[10.1007/s10584-011-0153-2](https://doi.org/10.1007/s10584-011-0153-2).
- Ilyina, T., K. D. Six, J. Segschneider, E. Maier-Reimer, H. Li, and I. Núñez-Riboni (2013), Global ocean biogeochemistry model HAMOCC: Model architecture and performance as component of the MPI-Earth system model in different CMIP5 experimental realizations: The Model Hamocc within Mpi-Esm in Cmp5. *Journal of Advances in Modeling Earth Systems*, **5**, 287–315, doi:[10.1029/2012MS000178](https://doi.org/10.1029/2012MS000178).
- Jones, C., et al. (2013), Twenty-First-Century Compatible CO<sub>2</sub> Emissions and Airborne Fraction Simulated by CMIP5 Earth System Models under Four Representative Concentration Pathways. *Journal of Climate*, **26**, 4398–4413, doi:[10.1175/JCLI-D-12-00554](https://doi.org/10.1175/JCLI-D-12-00554).
- Jones, C. D., M. Collins, P. M. Cox, and S. A. Spall (2001), The Carbon Cycle Response to ENSO: A Coupled Climate–Carbon Cycle Model Study. *Journal of Climate*, **14**, 17, doi:[10.1175/1520-0442\(2001\)014<4113:TCCRTE>2.0.CO;2](https://doi.org/10.1175/1520-0442(2001)014<4113:TCCRTE>2.0.CO;2).
- Kay, J. E. et al. (2015), The Community Earth System Model (CESM) Large Ensemble Project: A Community Resource for Studying Climate Change in the Presence of Internal Climate Variability. *Bulletin of the American Meteorological Society* **96**, 1333–1349, doi:[10.1175/BAMS-D-13-00255.1](https://doi.org/10.1175/BAMS-D-13-00255.1).

- 761 Lawrence, P. J. et al. (2012), Simulating the Biogeochemical and Biogeophysical Impacts of  
 762 Transient Land Cover Change and Wood Harvest in the Community Climate System  
 763 Model (CCSM4) from 1850 to 2100. *J. Climate*, 25, 3071–3095, doi:10.1175/JCLI-D-11-  
 764 00256.1.
- 765 Le Quéré, C., et al. (2013), The global carbon budget 1959–2011. *Earth System Science Data*, 5,  
 766 165–185, doi:[10.5194/essd-5-165-2013](https://doi.org/10.5194/essd-5-165-2013).
- 767 —, et al. (2018a), Global Carbon Budget 2017. *Earth System Science Data*, **10**, 405–448,  
 768 doi:[10.5194/essd-10-405-2018](https://doi.org/10.5194/essd-10-405-2018).
- 769 —, et al. (2018b), Global Carbon Budget 2018. *Earth System Science Data*, **10**, 2141–2194,  
 770 doi:[10.5194/essd-10-2141-2018](https://doi.org/10.5194/essd-10-2141-2018).
- 771 Li, H., and T. Ilyina (2018), Current and Future Decadal Trends in the Oceanic Carbon Uptake  
 772 Are Dominated by Internal Variability. *Geophysical Research Letters*, **45**, 916–925,  
 773 doi:[10.1002/2017GL075370](https://doi.org/10.1002/2017GL075370).
- 774 Maher, N., et al. (2019), The Max Planck Institute Grand Ensemble: Enabling the Exploration of  
 775 Climate System Variability. *Journal of Advances in Modeling Earth Systems*, **11**, 2050–  
 776 2069, doi:[10.1029/2019MS001639](https://doi.org/10.1029/2019MS001639).
- 777 Mankin, J. S., F. Lehner, S. Coats, and K. A. McKinnon (2020), The Value of Initial Condition  
 778 Large Ensembles to Robust Adaptation Decision-Making. *Earth's Future* 8,  
 779 doi:[10.1029/2020EF001610](https://doi.org/10.1029/2020EF001610).
- 780 Marsland, S. J., H. Haak, J. H. Jungclaus, M. Latif, and F. Röske (2003), The Max-Planck-  
 781 Institute global ocean/sea ice model with orthogonal curvilinear coordinates. *Ocean*  
 782 *Modelling*, 5, 91–127, doi:[10.1016/S1463-5003\(02\)00015-X](https://doi.org/10.1016/S1463-5003(02)00015-X).
- 783 Meinshausen, M., et al. (2017), Historical greenhouse gas concentrations for climate modelling  
 784 (CMIP6). *Geoscientific Model Development*, **10**, 2057–2116, doi:[10.5194/gmd-10-2057-](https://doi.org/10.5194/gmd-10-2057-2017)  
 785 [2017](https://doi.org/10.5194/gmd-10-2057-2017).
- 786 Millar, R. J. et al. (2017), Emission budgets and pathways consistent with limiting warming to  
 787 1.5 °C. *Nature Geoscience* **10**, 741–747, doi:[10.1038/ngeo3031](https://doi.org/10.1038/ngeo3031).
- 788 Milinski, S., N. Maher, and D. Olonscheck (2020), How large does a large ensemble need to be?  
 789 *Earth System Dynamics*, **11**, 885–901, doi:[10.5194/esd-11-885-2020](https://doi.org/10.5194/esd-11-885-2020).
- 790 Pongratz, J., C. H. Reick, R. A. Houghton, and J. I. House (2014), Terminology as a key  
 791 uncertainty in net land use and land cover change carbon flux estimates. *Earth System*  
 792 *Dynamics*, 5, 177–195, doi:[10.5194/esd-5-177-2014](https://doi.org/10.5194/esd-5-177-2014).  
 793
- 794 Poulter, B., et al. (2014), Contribution of semi-arid ecosystems to interannual variability of the  
 795 global carbon cycle. *Nature*, **509**, 600–603, doi:[10.1038/nature13376](https://doi.org/10.1038/nature13376).
- 796 Reick, C. H., T. Raddatz, V. Brovkin, and V. Gayler (2013), Representation of natural and  
 797 anthropogenic land cover change in MPI-ESM. *Journal of Advances in Modeling Earth*  
 798 *Systems*, 5, 459–482, doi:[10.1002/jame.20022](https://doi.org/10.1002/jame.20022).
- 799 Roeckner, E., Giorgetta, M. A., Crueger, T., Esch, M. and Pongratz, J. (2010), Historical and  
 800 future anthropogenic emission pathways derived from coupled climate-carbon cycle  
 801 simulations. *Climatic Change* **105**, 91–108, doi:[10.1007/s10584-010-9886-6](https://doi.org/10.1007/s10584-010-9886-6).

- Rogelj, J. *et al.* (2016), Differences between carbon budget estimates unravelled. *Nature Clim Change* **6**, 245–252, doi:[10.1038/nclimate2868](https://doi.org/10.1038/nclimate2868).
- Schneck, R., C. H. Reick, and T. Raddatz (2013) Land contribution to natural CO<sub>2</sub> variability on time scales of centuries: Land Contribution to CO<sub>2</sub> Variability. *Journal of Advances in Modeling Earth Systems*, **5**, 354–365, doi:[10.1002/jame.20029](https://doi.org/10.1002/jame.20029).
- Scott, D. W. (2015), *Multivariate density estimation: theory, practice, and visualization*. John Wiley & Sons.
- Shapiro, S. S. and Wilk (1965), M. B. An Analysis of Variance Test for Normality (Complete Samples). *Biometrika* **52**, 591–611, doi:[10.2307/2333709](https://doi.org/10.2307/2333709).
- Sonntag, S., J. Pongratz, C. H. Reick, and H. Schmidt (2016), Reforestation in a high-CO<sub>2</sub> world —Higher mitigation potential than expected, lower adaptation potential than hoped for. *Geophysical Research Letters*, **43**, 6546–6553, doi:[10.1002/2016GL068824](https://doi.org/10.1002/2016GL068824).
- Stevens, B., *et al.* (2013), Atmospheric component of the MPI-M Earth System Model: ECHAM6: ECHAM6. *Journal of Advances in Modeling Earth Systems*, **5**, 146–172, doi:[10.1002/jame.20015](https://doi.org/10.1002/jame.20015).
- Suarez-Gutierrez, L., Müller, W. A., Li, C. and Marotzke, J. (2020), Hotspots of extreme heat under global warming. *Climate Dynamics* **55**, 429–447, doi:[10.1007/s00382-020-05263-w](https://doi.org/10.1007/s00382-020-05263-w).
- Taylor, K. E., Stouffer, R. J. and Meehl, G. A. (2012), An overview of CMIP5 and the experiment design. *Bulletin of the American Meteorological Society* **93**, 485–498, doi:[10.1175/BAMS-D-11-00094.1](https://doi.org/10.1175/BAMS-D-11-00094.1).
- UNFCCC (2015), *Paris Agreement*, Article 14.
- UNFCCC (2017), *Report of the Subsidiary Body for Scientific and Technological Advice on its forty-fifth session, held in Marrakech from 7 to 15 November 2016*.
- Thomson, A. M., *et al.* (2011), RCP4.5: A pathway for stabilization of radiative forcing by 2100. *Climate Change*, **109**, 77–94, doi:[10.1007/s10584-011-0151-4](https://doi.org/10.1007/s10584-011-0151-4).
- Walker, A. P. *et al.* (2021) Integrating the evidence for a terrestrial carbon sink caused by increasing atmospheric CO<sub>2</sub>. *New Phytologist* **229**, 2413–2445 (2021).
- Yue, C., Ciais, P., Houghton, R. A. and Nassikas, A. A. (2020), Contribution of land use to the interannual variability of the land carbon cycle. *Nature Communications* **11**, 3170, doi:[10.1038/s41467-020-16953-8](https://doi.org/10.1038/s41467-020-16953-8).
- Zhang, Y., M. P. Dannenberg, T. Hwang, and C. Song (2019), El Niño-Southern Oscillation-Induced Variability of Terrestrial Gross Primary Production During the Satellite Era. *Journal of Geophysical Research Biogeosciences*, **124**, 2419–2431, doi:[10.1029/2019JG005117](https://doi.org/10.1029/2019JG005117).
- Zhu, Z., S. Piao, T. Yan, P. Ciais, A. Bastos, X. Zhang, and Z. Wang (2018), The Accelerating Land Carbon Sink of the 2000s May Not Be Driven Predominantly by the Warming Hiatus. *Geophysical Research Letters*, **45**, 1402–1409, doi:[10.1002/2017GL075808](https://doi.org/10.1002/2017GL075808).

**Past and Future Climate Variability Uncertainties in the Global Carbon Budget using the MPI Grand Ensemble**

T. F. Loughran<sup>1</sup>, L. Boysen<sup>3</sup>, A. Bastos<sup>1,2</sup>, K. Hartung<sup>1,\*</sup>, F. Havermann<sup>1</sup>, H. Li<sup>3</sup>, J. E. M. S. Nabel<sup>3</sup>, W. A. Obermeier<sup>1</sup>, and J. Pongratz<sup>1</sup>

<sup>1</sup>Dept. of Geography, Ludwig Maximilian University, Munich, Germany.

<sup>2</sup>Max Planck Institute for Biogeochemistry, Jena, Germany.

<sup>3</sup>Max Planck Institute for Meteorology, Hamburg, Germany.

\*Now at: Deutsches Zentrum für Luft- und Raumfahrt, Institut für Physik der Atmosphäre, Oberpfaffenhofen, Germany.

**Contents of this file**

Figures S1  
Text S1 describing Figure S2  
Figures S2  
Figures S3  
Figures S4  
Figures S5  
Figures S6  
Figures S7

**Introduction**

The following document contains supporting text and figures for the analysis in the main article. The MPI-GE carbon budget is presented in various forms: there is an unstacked presentation of the budget terms (Figure S1), spatial maps of ensemble standard deviation (Figure S2), a budget composed using CMIP5 emissions (Figure S3), comparisons to the future emissions and the 2020 Global Carbon Budget (Figure S4), demonstration of the exceedance probability calculation (Figure S5 and S6) and the ensemble sub-sampling for terms not presented in the main text (Figure S7).

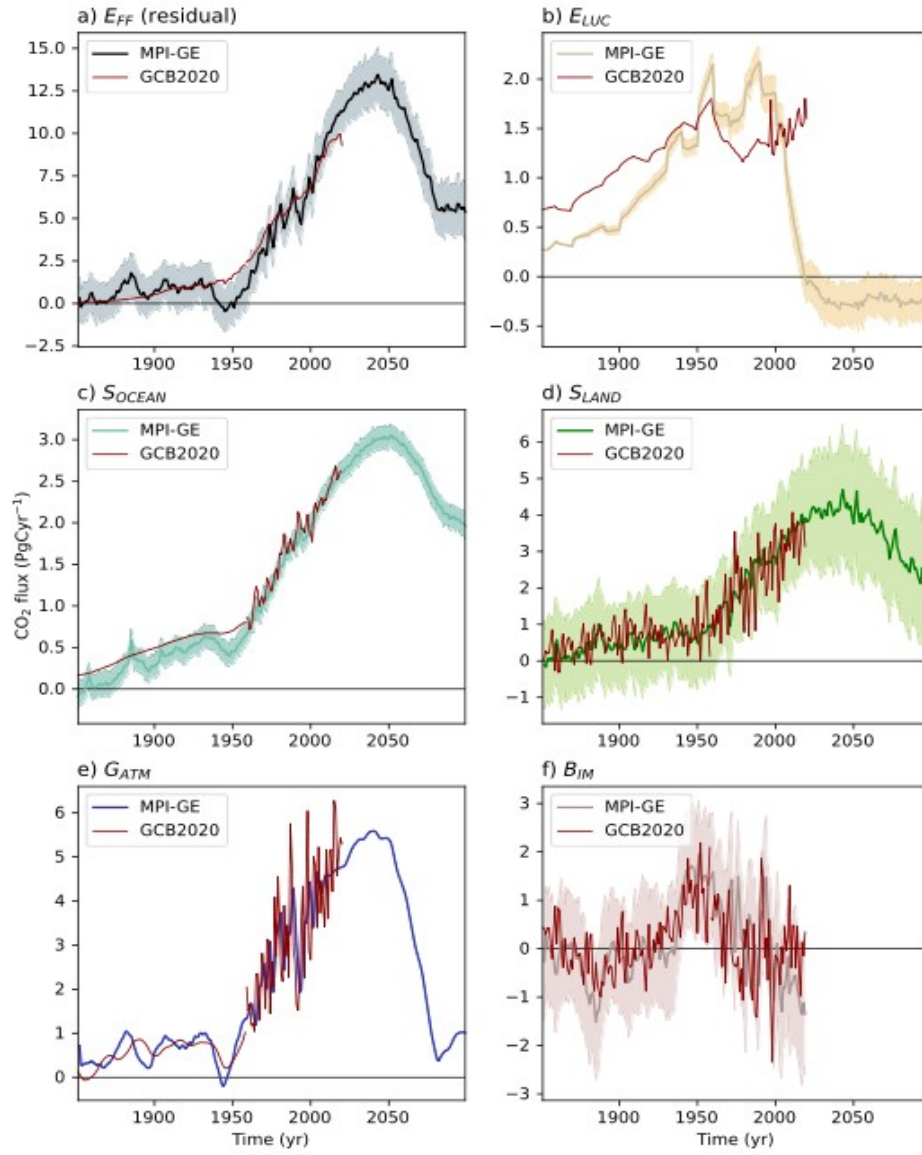


**Figure S1.** Unstacked MPI-GE carbon budget terms. The shaded region shows the  $\pm 1\sigma$  uncertainty range around the MPI-GE ensemble mean. The fine gray lines mark the corresponding GCB2020 budget terms. Panel f) shows the simulated  $B_{IM}$  term using the budget in Figure S3.



**Text S1.**

The spatial distribution of the standard deviation may reveal the regions of  $S_{\text{LAND}}$  and  $E_{\text{LUC}}$  that are most sensitive to changes in the climate under the RCP4.5 scenario. Figure S2 shows the standard deviation of  $S_{\text{LAND}}$  and  $E_{\text{LUC}}$  averaged over the last decade of the RCP4.5 scenario. The regions of  $S_{\text{LAND}}$  with the largest variations are tropical regions that can store large masses of carbon in particular in plant biomass (such as the Amazon region in South America, the Congo region in equatorial Africa, and Southeast Asia), and are also strongly influenced by ENSO. Vegetation in all of these regions is known to be sensitive to variations in climate modes (Dannenberg et al. 2015; Poulter et al. 2014; Zhang et al. 2019; Bastos et al. 2018). There are also moderate variances found in extra-tropical regions that are affected by internal climate variability, such as North America, Europe and Australia. Regions that are not sensitive to climate variations are the highly arid regions of Saharan Africa, Central Asia, and the boreal tundra regions. The distribution patterns of sensitivity are similar for  $E_{\text{LUC}}$  (since the cleared biomass is affected by internal climate variations in the same way as the biomass contributed by  $S_{\text{LAND}}$  is, although the magnitude of the variations are much smaller, and the largest values are focused on regions with high land-use change (which are scenario dependent). The  $E_{\text{FF}}$  and  $E_{\text{LUC}}$  are not directly affected by internal climate variations, but the historical exceedance probabilities are nonetheless presented in Figure S7.

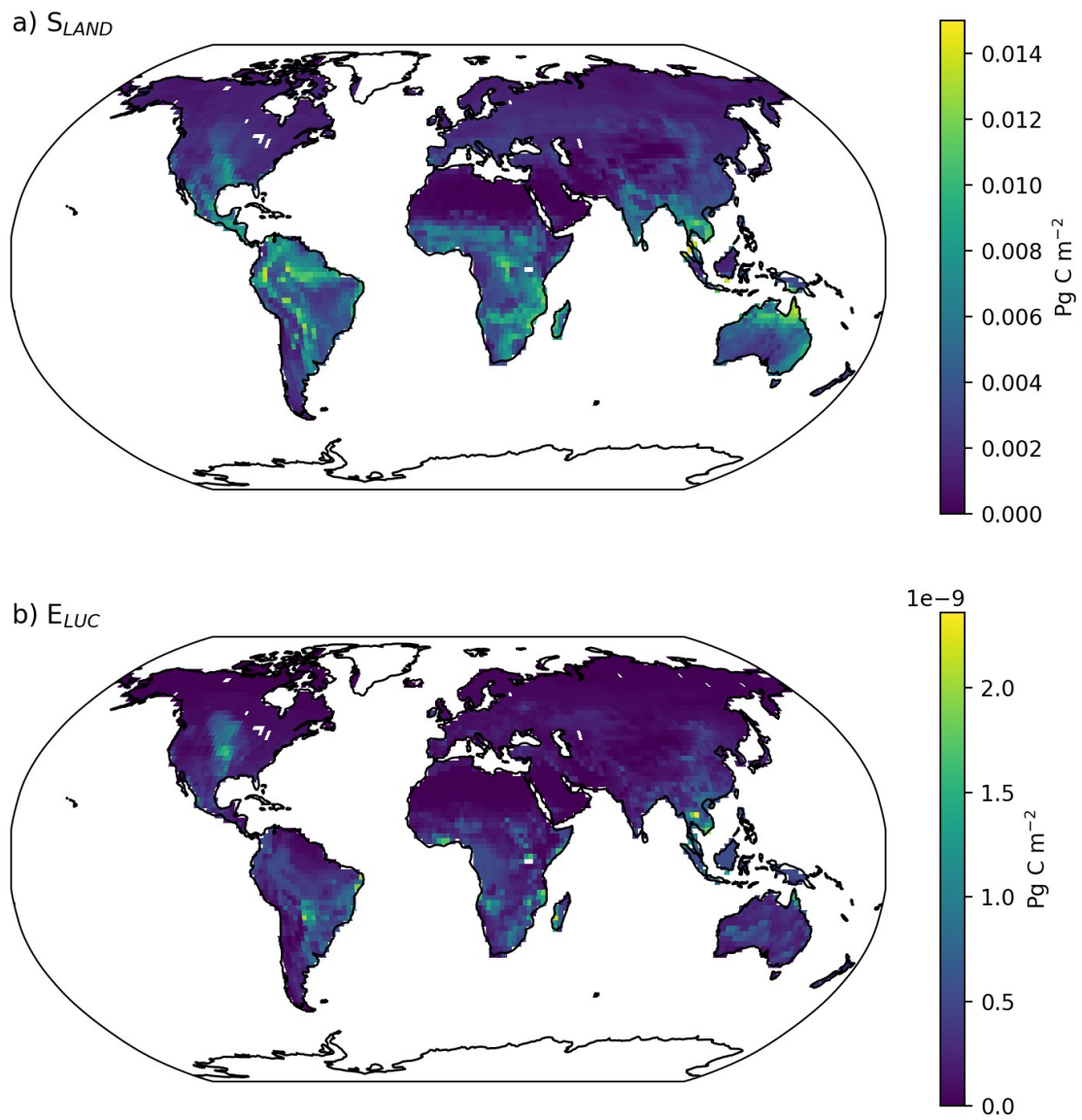


**Figure S2.** Maps of MPI-GE  $S_{LAND}$  and  $E_{LUC}$  standard deviation averaged for the final decade of the RCP4.5 scenario.



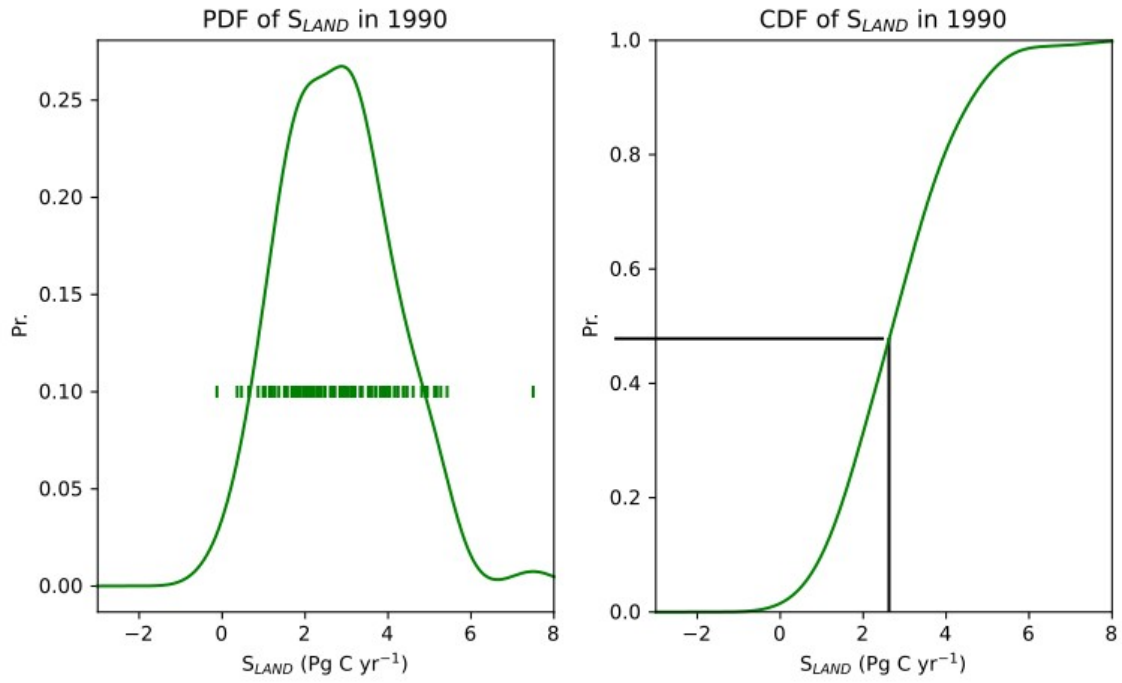


**Figure S3.** Probability of occurrence calculation of  $S_{LAND}$  for a single year 1990. The probability distribution function of the MPI-GE is on the left and the cumulative distribution function is on the right. Dots mark the  $S_{LAND}$  values for individual ensemble members. The 1990 GCB2020 value is the vertical line and it's corresponding cumulative probability of occurrence is the horizontal line.

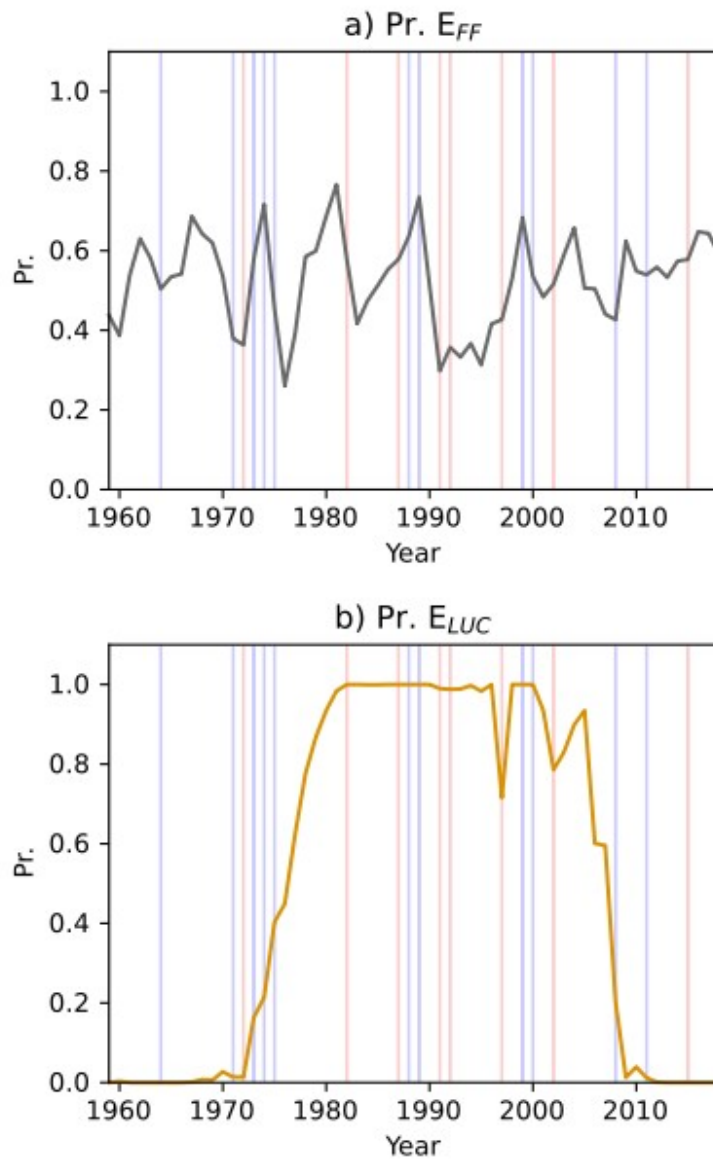


**Figure S4.** Probability of exceedance that the MPI-GE anthropogenic carbon fluxes are greater than the historical GCB2020 mean. The vertical lines mark El Niño (red) and La Niña (blue) years where Niño 3.4 index is greater than 1 standard deviation from the mean.

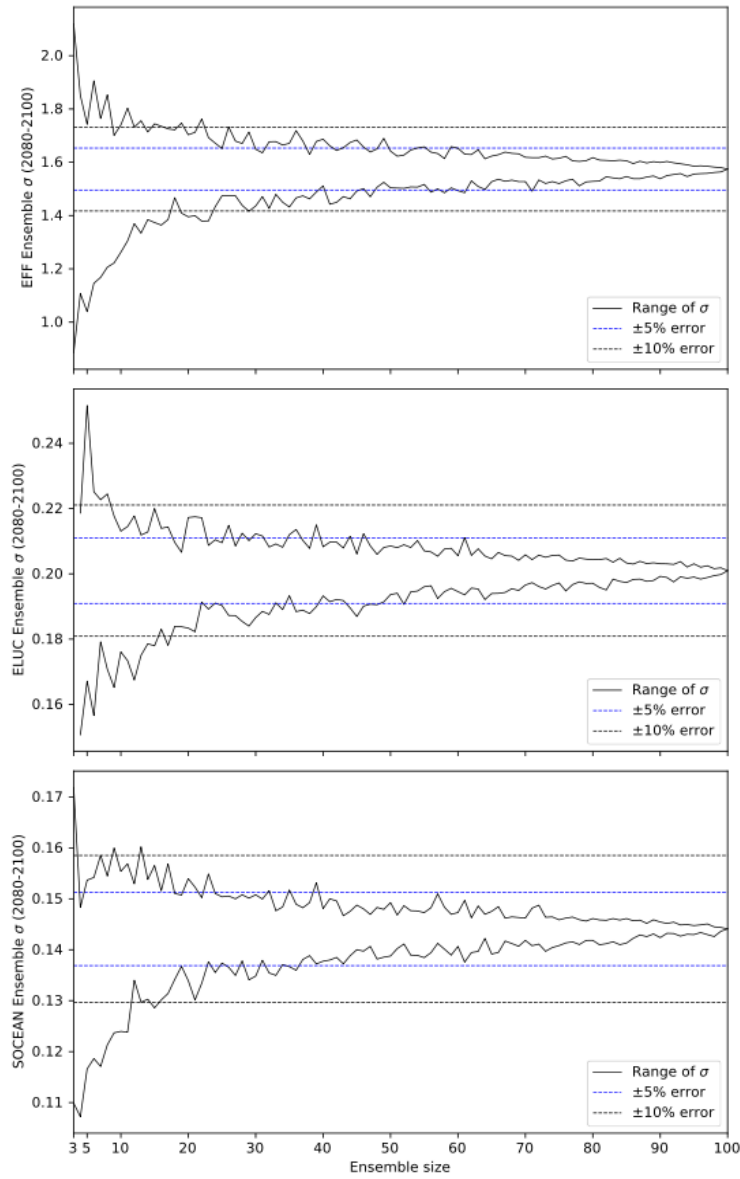


**Figure S5.** Range of standard deviation of the ensemble sub-samples for  $E_{FF}$  (top),  $E_{LUC}$  (middle) and  $S_{OCEAN}$  (bottom). Blue dashed lines mark the accuracy range of the subsample estimates for  $\pm 5\%$  error and the black dotted lines mark the accuracy range of the subsamples estimates for  $\pm 10\%$  error.

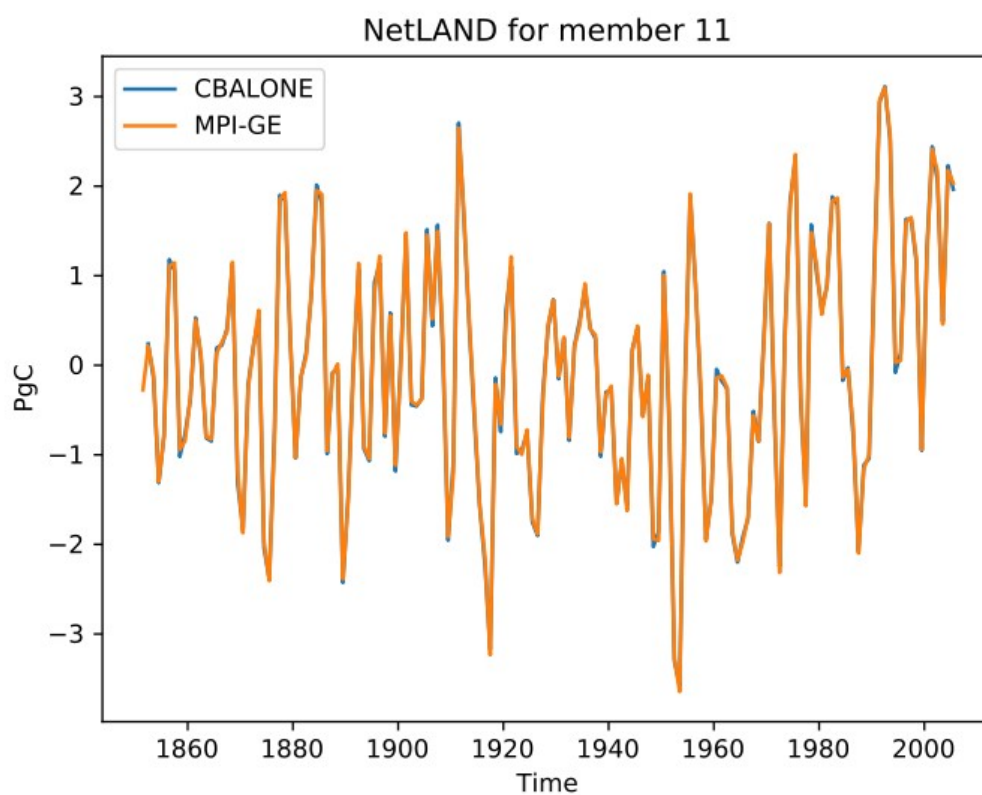


**Figure S6.** Net land-atmosphere exchange expressed as NBP for the historical period. MPI-GE and CBALONE with land use change are shown for comparison.